IN-34

02346

P-36

Elliptic Flow Computation by Low Reynolds Number Two-Equation Turbulence Models

(NASA-TM-105376) ELLIPTIC FLOW COMPUTATION
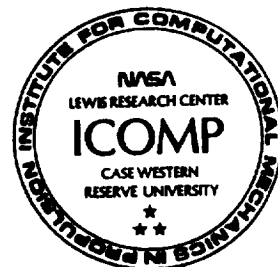BY LOW REYNOLDS NUMBER TWO-EQUATION
TURBULENCE MODELS (Alabama Univ.) ...

V. Michelassi and T.-H. Shih
Institute for Computational Mechanics in Propulsion
and Center for Modeling of Turbulence and Transition
Lewis Research Center
Cleveland, Ohio

December 1991

NASA
LEWIS RESEARCH CENTER
ICOMP
CASE WESTERN
RESERVE UNIVERSITY

NASA

Elliptic Flow Computation by Low Reynolds Number Two-Equation Turbulence Models

V. Michelassi* and T.-H. Shih
Institute for Computational Mechanics in Propulsion
and Center for Modeling of Turbulence and Transition
Lewis Research Center
Cleveland, Ohio 44135

Abstract

A detailed comparison of ten low-Reynolds-number $k - \epsilon$ models is carried out. The flow solver, based on an implicit approximate factorization method, is designed for incompressible, steady two-dimensional flows. The conservation of mass is enforced by the artificial compressibility approach and the computational domain is discretized using centered finite differences. The turbulence model predictions of the flow past a hill are compared with experiments at $Re = 1.4 \cdot 10^6$. The effects of the grid spacing together with the numerical efficiency of the various formulations are investigated. The results show that the models provide a satisfactory prediction of the flow field in the presence of a favourable pressure gradient, while the accuracy rapidly deteriorates when a strong adverse pressure gradient is encountered. A newly proposed model form that does not explicitly depend on the wall distance seems promising for application to complex geometries.

1 Introduction

The *direct numerical simulation* (DNS) of turbulent flows[13] is restricted to simple configurations and low Reynolds numbers (Re) because of the speed and memory limitations of supercomputers. A valid alternative, given by the *Reynolds averaging technique* of the Navier-Stokes equations with a model of Reynolds-stress, allows solving engineering problems with a manageable computer effort. Following the *Boussinesq assumption*, the Reynolds stresses are proportional to the mean velocity strain:

$$- \overline{u_i u_j} = \nu_t \left(\frac{\partial U_j}{\partial x_i} + \frac{\partial U_i}{\partial x_j} \right) - \frac{2}{3} k \delta_{ij} \tag{1}$$

---

*on leave from the University of Florence, Italy

in which $k = \frac{1}{2}\sum_{i=1}^{3}\overline{u_i u_i}$ is the turbulent kinetic energy, u_i the fluctuating velocity, U_i the mean velocity, ν_t is the so called *turbulent viscosity*, and the overbar stands for the average operator. The problem now is how to determine ν_t. With the local velocity and length scale of turbulence, ν_t can be modeled by the Kolmogorov expression:

$$\nu_t = c_\mu \frac{k^2}{\epsilon} \tag{2}$$

in which $\epsilon = \nu\overline{u_{i,j}u_{i,j}}$ is the dissipation rate of turbulent kinetic energy. The quantities k and ϵ will be determined by corresponding transport equations.

This approach has been applied to a very wide class of two dimensional and three dimensional compressible and incompressible flows[20]. Most of the applications use the *high Re form* of the turbulence models in which the effect of molecular viscosity is neglected and the presence of solid walls is accounted for by means of so called *wall functions*[11]. The model equations have been tuned using a set of experimental channel data obtained in the absence of strong pressure gradient.

As pointed out by Bradshaw[3], the effect of streamline curvature, induced by a pressure gradient not aligned with the main flow direction, is not properly accounted for in these models. Problems are even more evident in the case of separation since the wall function approach is strictly valid only for attached shear layers provided that the turbulence is in local equilibrium in the wall proximity. Several authors, among them Rodi and Scheuerer [22], showed that standard two equation models fail to reproduce the correct flow pattern in the case of adverse pressure gradients. Although the limitations of these models are well known, their better performance may be obtained by proper modeling of the viscous and buffer layers, which are usually bridged by wall functions.

With this in mind new formulations of the two-equation models, called *low Re forms (LR)* have been introduced in the past several decades. These models account for the molecular viscosity which is not negligible in wall regions, the normal velocity fluctuation damping induced by a solid boundary, and the presence of a anisotropic contribution to the dissipation rate of turbulence that dominates in the viscous layer[19, 24]. In the *LR* models the turbulence quantities are solved throughout the viscous and buffer layers thereby accounting for convection and diffusion in the molecular viscosity dominated region. The *LR* forms have been further tuned to fit the experimental data in the viscous and buffer layers, but, because of the difficulties in performing measurements in the wall proximity, the models have been often made to reproduce measurements with a very wide uncertainty range. Thanks to the recent availability of *DNS* results, although limited to very simple flows and quite low Reynolds numbers, it has been possible to formulate new *LR* models that are consistent with these numerical data sets. In a previous study by the authors[17], a new model has been compared with several other *LR* forms. The preliminary investigation was carried out by comparing the model predictions with *DNS* of a fully developed channel flow. In the present paper the attention will be focused on *LR* forms applied to a more complex geometry in the presence of streamline curvature and separation to highlight the differences in the various models. From a computational point of view it is important to observe that this investigation is carried out using a single solver able to cope with all the models thereby ensuring the same degree of accuracy

in the solution of the various model equations. Together with the turbulence models, the implicit solver will be briefly described in the following.

2 Selection of the $k - \epsilon \, LR$ models

The investigation carried out in ref.[17] includes ten models which are: Chien[4], (ch), Jones and Launder[9], (jl), Nagano and Hishida[18], (nh), Coakley[6], (co), Speziale et al.[25], (sp), Kim[8], (ki), Rodi[21], (ro), Lam and Bremhorst[10], (lb), Shih[23], (sh), Michelassi and Shih[17], (ms). The letter codes in parenthesis will be used to refer to each model. All these models are further tested in this study.

It is possible to express the LR models in a unified form using the following nondimensional variables (the overbar stands for a nondimensional quantity):

$$\bar{k} = \frac{k}{U^2} \qquad \bar{\epsilon} = \frac{\epsilon \, L}{U^3} \qquad \bar{\nu}_t = \frac{\nu_t}{\nu} \qquad \overline{U} = \frac{U}{U} \qquad \bar{x}_i = \frac{x_i}{L}$$

in which U is a typical velocity, L is a typical length, and ν is the fluid molecular viscosity. Accordingly, the flow Reynolds number is defined as:

$$Re = \frac{L \, U}{\nu}$$

Hereafter the variables will appear only in their nondimensional form so that the overbar will be dropped for simplicity. The turbulence model transport equations may be written as follows:

$$
\begin{cases}
\frac{\partial k}{\partial t} + \frac{\partial U_i k}{\partial x_i} = \frac{1}{Re} \left(\frac{\partial}{\partial x_i} \left(1 + \frac{\nu_t}{\sigma_k} \right) \frac{\partial k}{\partial x_i} \right) + P - \epsilon + D + \Pi \\
\frac{\partial \epsilon}{\partial t} + \frac{\partial U_i \epsilon}{\partial x_i} = \frac{1}{Re} \left(\frac{\partial}{\partial x_i} \left(1 + \frac{\nu_t}{\sigma_\epsilon} \right) \frac{\partial \epsilon}{\partial x_i} \right) + c_1 f_1 \frac{\epsilon}{k} P - c_2 f_2 \frac{\epsilon \tilde{\epsilon}}{k} + E
\end{cases}
\tag{3}
$$

in which

$$P = \frac{1}{Re} \nu_t \left(\frac{\partial U_i}{\partial x_j} \right) \left(\frac{\partial U_j}{\partial x_i} + \frac{\partial U_i}{\partial x_j} \right)$$

is the production rate, and

$$\nu_t = Re \, c_\mu \, f_\mu \, \frac{k^2}{\tilde{\epsilon}} \tag{4}$$

is the Kolmogorov expression for the turbulent viscosity modified by including the function f_μ. The extra terms D, E, Π represent the corrections to the standard high Re formulation. They allow balancing the transport equations (3) in the wall region[19]. Their detailed forms are listed in Table 2, and here,

$$\tilde{\epsilon} = \epsilon - D \tag{5}$$

In the $q - \omega$ model ($q = \sqrt{k}$, $\omega = \frac{\epsilon}{k}$) and the $k - \tau$ model ($\tau = \frac{k}{\epsilon}$), the transport equations of ω and τ are introduced instead of the ϵ equation.

The ro two-equation and ki four-equation models are $two\text{-}layer$ models in which an inner layer is defined close to the wall ($y^+ \leq 100$) where, while using a transport

model	f_μ	f_1	f_2
ch	$1 - exp(-.0115y^+)$	1.0	$1 - 0.22exp(-\frac{R_t^2}{36})$
jl	$exp\left(\frac{-2.5}{1+\frac{R_t}{50}}\right)$	1.0	$1 - 0.3exp(-R_t^2)$
nh	$(1 - exp(-\frac{y^+}{26.5}))^2$	1.0	$1 - 0.3exp(-R_t^2)$
co	$1 - exp(-.0065R_y)$	1.0	1.0
sp	$(1 + \frac{3.45}{\sqrt{Re_t}} \cdot tanh(\frac{y^+}{70}))$	1.0	$1 - 0.22exp(-\frac{R_t^2}{36})$
ki	$1 - exp(-.025\sqrt{R_t} - 10^{-5}R_t^2)$	1.0	1.0
ro	$1 - exp(-.0198R_y)$	1.0	1.0
lb	$(1 - exp(-.0165R_k))^2 \cdot (1 + \frac{20.5}{R_t})$	$(1 + \frac{.05}{f_\mu})^2$	$1 - exp(-R_t^2)$
sh	$1 - exp(-\sum_{i=1}^4 \alpha_i y^{+^i})$	1.0	$1 - 0.22exp(-\frac{R_t^2}{36})$
ms	$1 - \frac{exp(-.0004\cdot exp(1.2R_L))}{exp(-.0004)}$	1.0	$1 - 0.22exp(-\frac{R_t^2}{36})$

Table 1: **Damping functions in the LR forms**

equation to compute the turbulent kinetic energy, the dissipation rate is computed by an algebraic expression which is a function of the wall distance y and turbulent kinetic energy k. This choice allows removing most of the numerical problems usually connected with the LR forms in the wall region. However, the *two-layer* models have to properly deal with the problem of matching the inner layer with the outer layer in which different sets of equations hold. ki and ro use similar criteria to pass from the inner layer to the outer layer equations; the interface is placed at $\nu_t/\nu \approx 35 - 36$. Although k is solved by using the same transport equation in both the layers, the dissipation rate ϵ comes from an algebraic expression within the buffer layer and from a transport equation in the outer layer.

2.1 The damping functions

The damping functions selected in the various formulations may be found in table 1, whereas table 2 gives all the selected forms for the extra terms D, E, Π. Most of the models have a set of damping functions closely related to the Van Driest expression for the mixing length, L:

$$L = y \left(1 - e^{-y^+/26}\right)$$

where y^+ is

$$y^+ = u_\tau y Re \qquad (6)$$

The turbulent Reynolds numbers based on y, $R_y = \sqrt{k} y Re$, or $R_t = \frac{k^2 Re}{\epsilon}$ are also used to mimic effects of the wall. In nearly all the formulations under investigation the decay of the dissipation rate is governed by the exponential function f_2 proposed by Hanjalic and Launder[7], according to which c_2 has a finite value at the wall. The sp formulation needs an additional function to further damp the value of c_2 in the wall region (see ref.[25]). The empirical constant c_1 is left unchanged all the way to the wall in all the formulations with the exception of lb where, since no extra terms

model	II	D	E
ch	0	$-\frac{2}{Re}\frac{k}{y^2}$	$\frac{-2\epsilon}{Re\,y^2}exp(-.5y^+)$
jl	0	$-\frac{2}{Re}\left(\frac{\partial\sqrt{k}}{\partial y}\right)^2$	$-\frac{2\nu_t}{Re^2}\left(\frac{\partial^2 U}{\partial y^2}\right)^2$
nh	0	$-\frac{2}{Re}\left(\frac{\partial\sqrt{k}}{\partial y}\right)^2$	$-\frac{\nu_t}{Re^2}(1-f_\mu)\left(\frac{\partial^2 U}{\partial y^2}\right)^2$
co	0	0	—
sp	0	—	—
ki	0	—	—
ro	0	—	—
lb	0	0	0
sh	$\left[\frac{0.05}{f_\mu(1-exp(-y^+))}\frac{\mu_t}{\sigma_k}k_{,j}\right]_{,j}$	0	$-\frac{\nu_t}{Re^2}\left(\frac{\partial^2 U}{\partial y^2}\right)^2$
ms	$\left[\frac{0.004}{f_\mu^2}\frac{\mu_t}{\sigma_k}k_{,j}\right]_{,j}$	0	$-\frac{\nu_t}{Re^2}\left(\frac{\partial^2 U}{\partial y^2}\right)^2$

Table 2: **Extra terms in the LR forms**

are added in both k and ϵ, the production of dissipation rate must be damped in order to balance the ϵ equation at the wall.

The choice of the damping functions depends on the limiting behavior of turbulence near the wall. A correct formulation should fulfill the following relations:

$$U = o(y) \quad k = o(y^2) \quad \epsilon = o(1)$$

$$\tilde{\epsilon} = o(y^2) \quad \mu_t = o(y^3) \quad \overline{uv} = o(y^3)$$

together with a negative slope of the dissipation rate in the wall region. The two equation model proposed by Shih[23] matches the limiting forms remarkably well, but suffers numerical problems caused by $\tilde{\epsilon}$. In sh the decay of dissipation rate is

$$- c_2 f_2 \frac{\epsilon\tilde{\epsilon}}{k} \tag{7}$$

which is of $o(1)$ at the wall. The turbulent viscosity is computed as

$$\nu_t = c_\mu f_\mu Re \frac{k^2}{\tilde{\epsilon}} \tag{8}$$

in which the damping function f_μ is based on a fourth order polynomial of y^+. The $\tilde{\epsilon}$, needed in equations (7,8), is computed as

$$\tilde{\epsilon} = \epsilon - \frac{\left(\frac{\partial k}{\partial y}\right)^2}{2\,k\,Re} \tag{9}$$

This expression gives $\tilde{\epsilon} = o(y^2)$ at the wall. To avoid the convergence problems caused by unphysical overshoots of the second term on the right hand side of (9) near the wall (which causes negative dissipation rates), the ms model defines $\tilde{\epsilon}$ as

$$\tilde{\epsilon} = \epsilon f_\epsilon \tag{10}$$

5

where the f_ϵ function depends on the turbulent Reynolds number, $R_t = \frac{k^2 Re}{\epsilon}$:

$$f_\epsilon = f(R_t) = 1 - exp(-\sqrt{R_t})$$

At the wall, $R_t = o(y^4)$ so that the function f_ϵ is $o(y^2)$. Equation (10) prevents negative dissipation rates, and makes $\tilde{\epsilon} = o(y^2)$ at the wall. The f_ϵ function is designed to give $\tilde{\epsilon} \approx \epsilon$ for $y^+ \geq 6$.

Table 1 shows that all the LR forms, with the exception of jl and ms models, use damping functions for ν_t based on y or y^+, while f_2 is based on R_t. The use of y^+ as the exponent of the damping functions gives unphysical results in the case of stagnation points. In fact, the definition of the *friction velocity* u_τ appearing in equation (6) is:

$$u_\tau = \sqrt{\frac{\tau_{wall}}{\rho}}$$

$$\tau_{wall} = \mu \left(\frac{\partial U}{\partial n} \right)_{wall}$$

where n is the direction normal to the wall. At separation and reattachment points

$$\left(\frac{\partial U}{\partial n} \right)_{wall} \rightarrow 0$$

and $y^+ \rightarrow 0$ regardless of the value of y. This implies that f_μ is zero all along the flow section making the viscous layer thickness unphysically unbounded. There are several known *tricks* to overcome this problem, like relating u_τ to the k peak in the viscous layer via the wall function for the turbulent kinetic energy, or replacing the velocity gradient by the maximum value of the vorticity ω in the cross flow direction. While these and other tricks remove the singularity, they are both arbitrary and potential sources of inaccuracies. Moreover, a general turbulence model should not require information about the flow domain geometry, like the wall distance. The authors[17] have shown that, although the replacement of y^+ is not an easy task, it is possible to use the ratio R_L of the turbulence length scale L and the viscous length scale L_ν defined as

$$\left. \begin{array}{l} L = \frac{k^{\frac{3}{2}}}{\epsilon} \\ L_\nu = \frac{\nu}{|\tilde{U}|} \end{array} \right\} \rightarrow R_L = \frac{L}{L_\nu} \tag{11}$$

R_L approaches zero at the wall because $L \rightarrow 0$, $L_\nu \rightarrow \infty$, and reaches asymptotically a maximum in the log-law region. In the wall region the following limiting forms hold:

$$\left. \begin{array}{l} L = o(y^3) \\ U = o(y) \end{array} \right\} \rightarrow R_L = o(y^4)$$

Accordingly, the exponent of the damping function must be $R_L^{\frac{1}{4}}$ to give $f_\mu = o(y)$ at the wall. The final form of f_μ is:

$$f_\mu = 1 - \frac{1}{exp(-c_{\mu 1})} \cdot exp\left(-c_{\mu 1}\, exp\left(c_{\mu 2}\, R_L^{1/4} \right) \right) \tag{12}$$

6

in which $c_{\mu 1}$ and $c_{\mu 2}$ are two empirical constants. The application of ms to a fully developed channel flow[17] showed a much better agreement with DNS than the jl model. For any further detail about the models, the reader is referred to the original bibliography.

3 The implicit factored solver

The strong non-linearities usually associated with the LR forms require a robust implicit solver to avoid stringent stability limits. Among the several possibilities, the implicit approximate factorization by Beam and Warming[2] proved adequate for implementation in complex flows[15]. To take full advantage of the implicit time marching procedure for incompressible flows, the mass conservation equation, that does not contain time derivatives, has been modified according to the *artificial compressibility* approach originally developed by Chorin[5]. The corrected form of the continuity equation reads:

$$\frac{1}{\rho} \cdot \frac{\partial p}{\partial t} + \omega \frac{\partial U_i}{\partial x_i} = 0$$

in which $p = \rho \omega$ is an artificial equation of state and ω is the artificial compressibility parameter. The formulation ensures mass conservation only when a steady solution is reached and, consequently, $\frac{\partial p}{\partial t} \to 0$, thereby making it impossible to follow a physical time transient.

In two dimensions, the artificial compressibility, momentum, and transport equations for ϵ and k may be written in vector form:

$$\frac{\partial Q}{\partial t} + \frac{\partial E_c}{\partial x} + \frac{\partial F_c}{\partial y} = \frac{\partial E_v}{\partial x} + \frac{\partial F_v}{\partial y} + H \tag{13}$$

where the unknown vector is $Q = (p, U, V, \epsilon, k)^T$, E_c, F_c are convective terms, E_v, F_v are diffusive terms, and H gathers the sink-source terms. The full forms of the linearization for the artificial compressibility algorithm may be found in ref. [15]. In order to be able to cope with any geometry, the transport equations are discretized in a generalized curvilinear nonorthogonal coordinate system. The differencing stencil is

$$\frac{\partial}{\partial x_i} = \frac{\partial}{\partial \xi} \xi_{x_i} + \frac{\partial}{\partial \eta} \eta_{x_i}$$

where x_i are the $2 - d$ cartesian coordinates and ξ, η are the $2 - d$ curvilinear coordinates. Fluxes are computed by using conservative centered finite differences.

The implicit factored solver for a system of partial differential equations is based on a time linearization of the spatial operators. Since the *artificial compressibility* precludes following a physical time transient, the approximate factorization is implemented in its one step version that is first order accurate in time. The final form of the factored solver is

$$\begin{cases} \left(I + \theta \Delta t \left[-\alpha_\xi H_j + \frac{\partial(A + R_\xi)}{\partial \xi} - \frac{\partial^2 R}{\partial \xi^2}\right]\right) \cdot \Delta Q^* = RHS \\ \left(I + \theta \Delta t \left[-\alpha_\eta H_j + \frac{\partial(B + T_\eta)}{\partial \eta} - \frac{\partial^2 T}{\partial \eta^2}\right]\right) \cdot \Delta Q = \Delta Q^* \end{cases} \tag{14}$$

7

in which $RHS = \Delta t \left(-\frac{\partial E_c}{\partial x} - \frac{\partial F_c}{\partial y} + \frac{\partial E_v}{\partial x} + \frac{\partial F_v}{\partial y} + H \right)$, A, B are the convective Jacobians, R, T are the diffusive Jacobians, H_j is the source Jacobian, and $\Delta Q = Q^{t+1} - Q^t$. The solution process requires the direct inversion of block tridiagonal matrices.

Particular attention was devoted to the local time step formula. A conservative expression was obtained by computing the eigenvalues Λ of the convective Jacobian:

$$\Lambda_d^{(continuity)} = U_d$$

$$\Lambda_d^{(x-momentum)} = U_d + a_\omega \cdot R_d$$

$$\Lambda_d^{(y-momentum)} = U_d - a_\omega \cdot R_d$$

where $R_d^2 = d_x^2 + d_y^2$, $U_d = (U \, d_x + V \, d_y)$ is the unscaled contravariant velocity, $(d = \xi$ or $\eta)$, and a_ω is an artificial speed of sound defined as

$$a_\omega = \sqrt{\frac{U^2}{R_d^2} + \omega}$$

The local time step formula is:

$$\Delta t = \frac{CFL}{U_\xi + U_\eta + a_\omega \left(R_\xi + R_\eta \right)} \tag{15}$$

Equation (15) proved adequate for both $N - S$ and $k - \epsilon$ with CFL varying in the range $5 - 15$. No artificial damping terms are added to the right or left hand side. Any stability or pressure-velocity decoupling problem was solved by refining the computational grid or lowering the CFL in (15).

The time marching procedure updates the flow variables, p, U, V by solving the artificial compressibility equation. The $k - \epsilon$ equations are solved one at a time decoupled from the flow variables. In this manner the $k - \epsilon$ solution lags one time step with respect to the $N - S$ equations.

4   Linearization of source terms

The H_j Jacobian of the source term vector H, that appears in equation (14) is defined as

$$H_j = \frac{\partial H}{\partial Q}$$

While the derivation of the convective and diffusive Jacobians is a straightforward exercise, the choice of the linearization of H may play a significant role in the robustness of a turbulent flow solver. H can not be treated in a fully explicit way and, to maintain the stability of iterative procedure, it must be properly linearized. H_j is usually introduced in the sweep associated with the largest gradients, but in elliptic flows this direction is not always unique, so that it was found convenient to introduce

8

model	$\dfrac{\partial H_\epsilon}{\partial \epsilon}$	$\dfrac{\partial H_k}{\partial k}$
ch	$-2\,f_2\frac{\epsilon}{k} - \frac{E}{\epsilon}$	$-\frac{2}{Re\,y^2}$
jl	$-c_2\,f_2\frac{\epsilon}{k}$	$-\frac{\epsilon}{k}$
nh	$-c_2\,f_2\frac{\epsilon}{k}$	$-\frac{\epsilon}{k}$
co	$-2\,c_2\frac{\epsilon}{k} - \frac{k}{2}$	$-\frac{\epsilon}{2k}$
sp	$\frac{1-c_1}{k}\,P$	$-\frac{\epsilon}{k}$
ki	$-2\,c_2\frac{\epsilon}{k}$ $(for\ both\ \epsilon\ eq.)$	$-\frac{\epsilon}{k}$ $(for\ both\ k\ eq.)$
ro	$-2\,c_2\frac{\epsilon}{k}$	$-\frac{\epsilon}{k}$
lb	$-2\,c_2\frac{\epsilon}{k}$	$-\frac{\epsilon}{k}$
sh	$-c_2\,f_2\frac{\tilde{\epsilon}}{k}$	$-\frac{\epsilon}{k}$
ms	$-c_2\,f_2\frac{\tilde{\epsilon}}{k}$	$-\frac{\epsilon}{k}$

Table 3: **Approximate source Jacobian**

it in both the sweeps according to the directional weights α in equation (14). Typical values of α are $1 - 5$.

The source Jacobian H_j, if negative, improves the algorithm robustness by increasing the diagonal dominance of the tridiagonal block matrix. This observation indicates that the optimal form of H_j is not necessarily the exact differentiation of H, that may have positive and negative contributions, but an approximate form that is always negative. Possible numerical problems may be also caused by overshoots of H_j. In fact the tridiagonal matrix given by equation (14) is

$$A_{i-1} \cdot \Delta U_{i-1} + (H_j + A_i) \cdot \Delta U_i + A_{i+1} \cdot \Delta U_{i+1} = RHS_i$$

If $H_j \gg A$ and $H_j \gg RHS$, $\Delta U \to 0$ regardless of the value of RHS. This may unphysically freeze the local solution.

After intense numerical testing, we found it convenient to compute H_j dropping the positive terms. To prevent possible over- or under-shoots only the leading terms in the viscous layer were retained. They have been determined by substituting in k, ϵ, U their limiting forms at the solid boundary for each model. The linearization for the ten models may be found in table 3. The analysis of the source Jacobians of the formulations showed that all the models used in this paper have the same degree of the robustness with the exception represented by the lb model for which serious numerical problems were encountered.

5   Turbulent flow past a hill

The aforedescribed models have been compared for a fully developed channel flow [17]. The computed results showed significant discrepancies among the models and only few of the formulations proved to fit with the DNS data at $Re = 3300$. The very low Reynolds number and the simple geometry used for testing indicated that further investigation is necessary to verify the model performances in a complex geometry at very high Re, as often encountered in engineering applications.

9

grid #	points	st
1	111×81	1.08
2	125×121	1.07
3	221×121	1.07

Table 4: **Grids (st=stretch ratio)**

For incompressible two-dimensional flows with streamline curvature there are only a few valuable experimental data sets. Among these we chose the flow past a circular hill[1]. In this test an incoming boundary layer experiences a short region of concave curvature with adverse pressure gradient, prior to encountering a long region of convex curvature in which the pressure gradient reverts to favorable and then becomes adverse. At this point the measurements detect a small separated region downstream of the hill in correspondence to a short convex curvature of the lower boundary. This experiment provides an interesting opportunity to test the turbulence models in a mixed adverse-favorable pressure gradient condition. The flow approaches the hill with a thin boundary layer ($\delta = 55.7\,mm$). The reference velocity U_{ref} is approximately 20 m/s, which gives a Reynolds number based on the hill curvature radius ($= 1284\,mm$) approximately equal to $1.4 \cdot 10^6$.

The measurements include the skin friction coefficient, c_f, obtained by the Clauser chart and the Preston tube all along the hill together with the wall static pressure distribution, c_p. The two methods used to determine c_f did not give significantly different results.

The mean velocity, turbulent normal and shear stresses are measured in ten different sections along the hill. The mean velocities are measured by a Pitot tube accounting for displacement effects in the wall proximity. The turbulent stresses are measured by using normal and cross hot-wires. The cross sectional measurements are interrupted very close to separation: this prevents a detailed comparison in the region well inside the recirculation.

The computations have been carried out using the three grids summarized in table 4; figure 1 shows grid number 2. The stretch ratio st is defined as the ratio of two consecutive grid cell heights in the cross flow direction.

The grid height was twice the hill curvature radius to minimize the effect of the upper boundary on the solution, where a zero normal gradient condition was implemented. On the exit boundary, a zero gradient condition was found adequate provided that the computational domain was extended sufficiently downstream of the hill.

Because of the incoming boundary layer and the large Reynolds number, grid number 1 allowed placing the first grid point away from the wall at $y^+ \approx 9$, while with grids number 2 and 3 the points were more clustered at the wall to give $y^+ \approx 1$. Grid 3 was introduced to check whether a stronger mesh refinement could bring about further changes in the computed results. The computations showed that the converged results obtained with grid 2 were nearly indistinguishable from those obtained with grid 3, so that all the final calculations were carried out with grid 2.

The mean velocity and turbulence quantities at the inlet section of the computational domain were specified according to the experimental profiles at $s = 596$. An attempt to use a fully developed flow inlet condition revealed the extreme sen-

10

sitivity of the computed results to the incoming profiles. When the inlet boundary layer thickness or the turbulent kinetic energy did not match with measurements, the computed profiles were far off from experiments. Figure 2 shows the computed turbulent viscosity levels at $X = 1990\,mm$ for both the fully developed and experimental inlet conditions. The ν_t profiles differ by approximately one order of magnitude immediately outside of the buffer layer. This observation shows the stringent need for detailed inlet conditions to perform a meaningful computation.

5.1   Wall static pressure

First let us look at the static pressure, C_p, along the lower side of the computational domain. Figure 3 gives the computed C_p using grids 1 and 2 with various models.

The ch model shows a good fit with experiments in the adverse pressure gradient (apg) region corresponding to the positive peak in C_p. The peak is well captured by both the grids. The same degree of accuracy is maintained all along the favourable pressure gradient (fpg) region. When the gradient reverts to positive the two grids start to give different results. The coarse grid generally produces larger recirculations with a moderate pressure recovery downstream of the hill, but it completely fails to reproduce the other flow variables, whereas the refined grid number 2 predicts a stronger pressure recovery than that shown by experiments. Nearly all the models gave a shorter and thinner recirculation with the refined grid as compared to the coarse one. This is somewhat surprising, but the converged results clearly showed that a large reversed flow region was detected by using the coarse grid number 1 together with very thick boundary layers in contrast with experiments in which the boundary layer remains quite thin. The same excessive pressure recovery was also found by Kim[8].

The lb model seems to follow the experimental C_p distribution quite closely and clearly predicts the static pressure drop in the large separated region downstream of the hill. The grid independence is quite remarkable. Unfortunately this model caused serious numerical problems and the results with both grids 1 and 2 are only partially converged.

The nh model is very similar to the jl formulation. However, the two formulations give results considerably different for a fully developed channel flow at moderate Re. Figure 3 shows that the differences between the models fade out for a high Re flow provided that a refined grid is used. In fact when using a coarse grid the inaccuracies in the k and ϵ profiles directly affect the turbulent viscosity distribution via the f_μ function based on R_t. The same effect is clearly smeared when using f_μ based on y^+ which is much less sensitive to the local turbulent flow field. The differences between the coarse and the refined grid are larger in the adverse pressure gradient region in which the flow is likely to encounter the largest gradients. The direct comparison of these two models shows that, even if the replacement of the damping functions based on y^+ is desirable, the use of R_t introduces a strong mesh dependence and the use of a very refined grid becomes compulsory to obtain a reasonable static pressure distribution (typically, the first grid point away from the wall must be placed at $y^+ \approx 1$, as in grid 2, to have grid independent results).

The $q - \omega$ model introduced by Coakley, co, was found to give a poor fit with DNS of a channel flow[17]. Nevertheless, it succeeds in giving a satisfactory agreement with

the measured flow past a hill. The model appears to be very grid sensitive on account of the differences in the static pressure distribution in both the *apg* regions. The main reason for this is again the damping function f_μ which is based on R_y. As in the *jl* model, if the peaks of k and ϵ are not properly resolved, the inaccuracies will be felt also in the damping of the turbulent viscosity with large effects on the mean flow field.

The *sp* model fits remarkably well the experimental static pressure coefficient until the separated region is approached. Moreover the model seems relatively grid independent until the strong *apg* is reached. At this point *sp* behaves like the other formulations. The pressure recovery in the separated region is still too large, and, when comparing this model with the other LR forms that use the wall distance y, it is evident that *sp* does not bring about any considerable improvement.

The *sh* and *ms* forms are very similar and, when using the refined grid, the static pressure profiles are nearly indistinguishable. The introduction of the pressure transport term II does not seem to play a significant role in the determination of the static pressure. For these two models the effect of the damping function f_μ based on y^+ or R_t is even more evident. Let's recall that in *sh* the f_μ function is based on a fourth order polynomial of y^+, while *ms* uses a complex function of the turbulent Reynolds number. Since f_μ appears in both the turbulent viscosity formula and the pressure transport term, the *ms* model will be very grid dependent for the same reason that *jl* was found to be grid dependent. This feature of *ms* was not highlighted in the channel flow computations [17] because of the much less stringent mesh points requirement.

The two-layer models give results that are somewhat less grid sensitive than the other formulations. This is partly due to the algebraic dissipation rate equation in the wall proximity, which, if solved by a transport equation down to the wall, appears to have more stringent mesh requirements. Nevertheless *ro* and *ki* predictions are very similar to the other models in the first *apg* and *fpg* regions. Again, differences start to appear in the strong *apg* region prior to separation. Here, while *ro* shows a notable difference between the two grids, *ki* gives profiles remarkably grid independent. It seems that the two scale model serves to relax the grid requirement.

5.2 Skin friction

The skin friction coefficient, nondimensionalized with respect to the free stream dynamic pressure, exhibits a peak approximately corresponding to the top of the hill. It reverts to negative values downstream of the hill in the short region with convex curvature where separation takes place. The plots report only the skin friction coefficient, C_f, computed with the refined grid number 2.

The form of the *friction velocity* u_τ to be used in the damping functions based on y^+ is of primary importance for the skin friction coefficient. To avoid numerical problems caused by sudden changes in the turbulent viscosity, the friction velocity (mentioned in section 2.1) was related to the peak of turbulent kinetic energy closest to the wall via the standard wall function for k

$$u_\tau \approx \sqrt{k_{max}\sqrt{C_\mu}}$$

Small convex curvature can produce a significant reduction of the skin friction coefficient, whereas a concave curvature causes an increase in C_f. In the present case, the ratio δ/R, where R is the local curvature radius, is above 0.01 so that the curvature effect gives strong changes in the skin friction.

Figure 5 reports the comparison between the measured and computed distribution. The ch formulation shows a satisfactory agreement with the experimental data in both the apg and fpg regions. In the first apg region ch seems to reproduce the measurements quite well. The sudden inversion from apg to fpg gives a very thin boundary layer together with a dramatic increase in the skin friction. The behavior of C_f quite closely resembles that of the static pressure coefficient. The peak in C_f is located approximately at the static pressure minimum prior to inversion to apg. The separation point is not fixed by geometrical constraints and it results from the local boundary layer thickness and pressure gradient. The general tendency of the models was to locate the separation point downstream of the measured one which is at $X_s^{(exp)} \approx 2095\,mm$. ch locates the separation at $X_s \approx 2155\,mm$. The profile given by lb is far from the experimental results. Moreover lb locates a short recirculation upstream of the hill corresponding to a strong decelerated region at the static pressure maximum in contrast with measurements where no separation is detected. Nevertheless, the lb results, because of the aforementioned numerical problem, are only partially converged.

The jl and nh models give similar results. The separation point is located by both the models at $X_s \approx 2170\,mm$. The direct comparison of the two models allows evaluating the effect of the damping function f_μ based on R_t or on y^+. The low Re calculations of ref.[17] showed that the f_μ damping form selected in jl was suited only for high Re flows. In fact, in this test, it appears that the boundary layer is properly predicted together with the shape of the skin friction coefficient. On the other hand, the damping function in nh which requires y^+, does not perform as well as the one in jl, especially in the fpg region.

The formulation proposed by Coakley (co) is the only one that does not detect any reversed flow downstream of the hill. The DNS comparison for the channel flow[17] showed that co clearly overestimates the turbulent viscosity all along the cross section. This ends in producing excessive momentum diffusion and less or no separation at all. The sp model follows the measurement remarkably well in the fpg region and locates the separation point at approximately $X_s \approx 2150\,mm$. sp responds to apg with a dramatic drop in the skin friction. While this behavior is qualitatively correct, the C_f drop in both the apg regions is steeper than the experimental drop. This feature is in contrast with all the other models in which there is a tendency to closely follow the experimental skin friction.

The two formulations that account for the pressure transport term, Π, behave differently on account of the selected form of the damping function f_μ. While sh gives probably the best agreement with experiments, ms overestimates the skin friction peak by approximately 5%. The pressure transport term is more important in apg and, in fact, sh and ms seem to give an improved fit with experiments as soon as the pressure gradient reverts from favorable to adverse. The introduction of the pressure correlation in the transport of the turbulent kinetic energy proves here to have a beneficial effect on the prediction. Although further testing is necessary to draw a final conclusion, it seems that the modeling of Π as a turbulent kinetic energy diffusion is appropriate at least for this class of flows.

13

model →	ch	jl	nh	co	sp	ki	ro	lb	sh	ms
u	1	1	1	1	1	1	1	1	1	1
$\overline{u_i u_j}$	3	3	4	4	3	3	3	4	3	3
k	2	2	2	2	2	2	2	2	2	2

Table 5: **Exponents of the wall limiting forms.**

For the two-layer models the effect of the matching criteria on C_f was investigated. Figure 6 shows the interface distance from the wall for both ro and ki. The two models predict different turbulent viscosity levels in the buffer layer. In fact, while the automatic matching criteria was $\nu_t \approx 36$ for both models, this value of the turbulent viscosity is reached at a larger distance from the wall by ki than ro. Nevertheless, the difference is at most 0.1% of the hill curvature radius. Moreover this difference seems to be constant all along the hill shape and it qualitatively resembles the shape of the wall static pressure for both the models. The ro formulation fails to predict separation when fixing the matching point in the computational domain according to the experimental inlet profiles. Conversely, the separation point is remarkably well predicted at $X_s \approx 2095\,mm$ when letting the model adjust the matching level at $\nu_t \approx 36$ in accordance to the locally computed turbulent viscosity. The ro formulation has already proved to give larger separation bubbles with respect to other LR forms[14], and this test confirms this tendency. The reason for this is probably that in ro the dissipation rate is computed by using the Norris and Reynolds algebraic expression within the buffer layer which gave better results than the standard $k - \epsilon$ model in apg[22]. The results given by ki are similar.

5.3 Cross sections

In order to provide a complete view of the model performance, the mean velocity, turbulent kinetic energy, and turbulent shear stress profiles are reported in five different cross sections. The location of the five sections may be found in Fig.1. The results reported in this set of plots refer to grid number 2 only.

In table 5 all the ten models show similar limiting forms at the wall for the mean velocity and turbulent kinetic energy. Conversely, the turbulent shear stress modeled by nh, co, and lb is $o(y^4)$ at the wall, whereas the other models show $o(y^3)$.

Figure 7 reports the mean velocity profiles at the aforementioned five cross sections, while figures 8 and 9 show the turbulent shear stress and the turbulent kinetic energy respectively. The plots show a closeup view of the region close to the wall since the flow variables were nearly flat in the outer part of the domain.

The first section at $x = 596\,mm$ is not of particular interest since the disturbance given by the presence of the hill is not yet felt. Nevertheless, all the models agree with experiments within a narrow range, especially for velocity and turbulent shear stress profiles. It is observed that there is no $\overline{u_i u_j}$ inversion and that the turbulent shear stress reaches zero at $Y \approx 60$ for all the models. The computed turbulent kinetic energy is underestimated by all the models.

The second section at $X = 1183\,mm$ is of much more interest since it is located near the pressure gradient inversion immediately downstream of the beginning of

the long convex region. Both *ch* and *lb* fit the measured velocity profiles which show a very thin boundary layer caused by the presence of the obstacle. *jl* and *nh* seem to overestimate the boundary layer thickness. (*jl* produces a much stronger overestimation of the boundary layer thickness than *nh*).

The strong reduction of the boundary layer thickness results in a large mean strain in the viscous layer. This can be seen in the peak of the turbulent shear stress and turbulent kinetic energy located in the wall proximity. *jl* and *nh* show a strong k overshoot that is not found by the other models. In checking every single model term, this behavior appeared to be caused by the selected form of the extra destruction rate, D, that is proportional to the square of the turbulent kinetic energy gradient as follows

$$D \propto \left(\frac{\partial \sqrt{k}}{\partial y} \right)^2 \tag{16}$$

Equation (16) seems to produce k overshoots in *fpg* regions.

The third cross flow section, at $X = 1469\,mm$ is well inside the *fpg* region. With respect to the previous section the growth of the boundary layer is evident even if the overall velocity profile seems to be only weakly affected. The reduction of the turbulent shear stress is well predicted by all the models. *jl* and *nh* give overshoots in k and $\overline{u_i u_j}$, and qualitatively behave as in the previous section.

When moving to the fourth and fifth sections at $X = 1862\,mm$ and $X = 1990\,mm$ respectively, differences between the model predictions start to be more evident. In these sections the flow encounters a much stronger *apg* than that found before section 2. The predicted velocity profiles are in good agreement with measurements for nearly all the models. Nevertheless the velocity profiles predicted by *sh* and *ms* seem to be in slightly better agreement with experiments than those predicted by using the other models, especially at the edge of the boundary layer. All the models tend to overestimate $\overline{u_i u_j}$ although the shape of the measured turbulent shear stress is well predicted.

5.4 Numerical details

Sections 3 and 4 give some details about the solver structure that was left unchanged for all the models. In the calculations the turbulence field was implicitly updated at the end of every implicit $N - S$ sweep. No advantages were found in updating k and ϵ after a fixed number of $N - S$ sweeps. The computations were carried out on the *Cray YMP* computer at NASA Lewis Research Center. Converged results with the 125×121 grid were obtained after 2000 iterations in $\approx 500 - 600$ seconds. The slow convergence rate was caused by the lack of numerical damping terms and by the grid cell aspect ratio that reached several thousands.

The only LR form showing serious numerical instabilities was *lb*. The proposed linearization for the source terms, while preventing the code from blowing up, did not achieve the overall residual of the order of $10^{-6} - 10^{-7}$ that was requested for all the other models.

15

6 Concluding Remarks

The comparison of ten different LR two-equation models in a complex geometry shows the limits of these models. Despite the improvements in channel flow predictions (highlighted in a previous investigation[17]) introduced by the use of the low-Reynolds-number corrections to the high-Reynolds number two-equation model, problems occur when trying to model flows with strong pressure gradients and streamline curvature. The large differences among the model predictions for a simple channel flow at a moderate Reynolds number seem to fade out in such a complex geometry. The reason for that is not very clear. This may be, in part, due to the very high Reynolds number that reduces the overall influence of the LR model corrections. sh, and consequently ms, attempts to introduce an extra model term which is the pressure correlation Π in the k equation. The skin friction coefficient seems to be the only quantity affected by Π in response to the pressure gradients and the other flow variables appear to be only marginally influenced.

In addition, the ms model does not explicitly depend on the wall distance and yields comparable results with the best of the other two-equation models. This indicates its promise for modeling of complex turbulent flows.

When using a single solver to carry out calculations with different LR models the differences in the predictions must be attributed only to the model formulations. Consequently, the present set of tests gives some understanding of the model discrepancies that were hidden behind purely numerical differences.

References

[1] Baskaran, V.; Smits, A.J.; Joubert, P.N.: A Turbulent Flow over a Curved Hill, Part 1. Growth of an Internal Boundary Layer. *Journal of Fluid Mechanics*, Vol. 182, 1987, pp.47-83.

[2] Beam, R.M.; Warming, R.F.: Implicit Numerical Methods for th Compressible Navier-Stokes and Euler Equations. Lecture Notes, 1981-82 Lecture Series Programme, Computational Fluid Dynamics, von Karman Institute for Fluid Dynamics, Belgium, March 1982.

[3] Bradshaw, P.: Effects of Streamline Curvature on Turbulent Flow. AGARDograph 169, 1973.

[4] Chien, K.Y.: Predictions of Channel and Boundary-Layer Flows with a Low-Reynolds-Number Turbulence Model. *AIAA Journal*, Vol. 20, no.1, 1982, pp. 33-38.

[5] Chorin, A.J.: A Numerical Method for Solving Incompressible Viscous Flow Problems. *Journal of Computational Physics*, Vol.2, n.1, 1967, pp.12-26.

[6] Coakley, T.J.: Turbulence Modelling Methods for the Compressible Navier-Stokes Equations. *AIAA paper* 83-1693, 1983.

16

[7] Hanjalic, K.; Launder, B.E.: Contribution Towards a Reynolds Stress Closure for Low-Reynolds-Number Turbulence. *Journal of Fluid Mechanics* Vol. 74, 1976, pp.593-610.

[8] Kim, S.-W.: Numerical Investigation of an Internal Layer in Turbulent Flow Over a Curved Hill. NASA TM-102230, ICOMP-89-20.

[9] Jones, W.P.; Launder, B.E.: The Calculation of Low-Reynolds Number Phenomena with a Two-Equation Model of Turbulence. *International Journal of Heat and Mass Transfer*, Vol.16, 1973, pp. 1119-1130.

[10] Lam, C.K.G.; Bremhorst, K.: A Modified Form of the $k - \epsilon$ Model for Predicting Wall Turbulence. *Transaction of the ASME, Journal of Fluids Engineering*, Vol.103, September 1981, pp. 456-460.

[11] Launder, B.E.; Spalding, D.B.: The Numerical Computation of Turbulent Flows. *Comp. Math. App. Mech. Engg.*, Vol. 3, 1974, pp.269-289.

[12] Lumley, J.L.: Computational Modeling of Turbulent Flows. *Advances in Applied Mechanics*, Vol. 18, 1978, pp.123-176.

[13] Mansour N.N.; Kim J.; and Moin P.: Reynolds-stress and Dissipation-Rate Budgets in a Turbulent Channel Flow. *Journal of Fluid Mechanics* Vol. 194, 1988, pp.15-44.

[14] Michelassi, V.: Testing of Turbulence Models with an Artificial Compressibility Solution Method. Report SFB (Sonderforschungbereich, University of Karlsruhe) 210 T49, University of Karlsruhe, Karlsruhe, West Germany, January 1989.

[15] Michelassi, V.: Simulation Methods of Viscous Flows in Turbomachinery Channels (*in italian*). PhD thesis, Univeristy of Florence, Italy, 1990.

[16] Michelassi. V.; Martelli F.: Numerical Computation of Turbulent Flows by Low-Reynolds-Number Two-Equation Models. *Proceedings of the International Symposium on Engineering Turbulence Modelling and Measurements*, September 24-28, 1990, Dubrovnik, Yugoslavia.

[17] Michelassi, V.; Shih, T.H.: Low Reynolds Number Two-Equation Modelling of Turbulent Flows. NASA TM104368, ICOMP-91-06; CMOTT-91-01.

[18] Nagano, Y.; Hishida, M.: Improved Form of the $k - \epsilon$ Model for Wall Turbulent Shear Flows. *ASME Transactions, Journal of Fluid Engineering*, Vol. 109, 1987.

[19] Patel, V.C.; Rodi, W.; and Scheuerer, G.: Turbulence Models for Near-Wall and Low Reynolds Number Flows: A Review. *AIAA Journal*, Vol. 23, no. 9, 1985, pp. 1308-1319

[20] Rodi, W.: Turbulence Models and their Application in Hydraulics. International Association of Hydraulic Research, Monograph, Delft, The Netherlands, 1980.

[21] Rodi, W.: Recent Developments in Turbulence Modelling. *Proceedings, Third International Symposium on Refined Flow Modelling and Turbulence Measurements*, July 1988, Tokyo, Japan.

17

[22] Rodi, W; and Scheuerer, G.: Scrutinizing the $k - \epsilon$ model under adverse pressure gradient conditions. *ASME Transactions, Journal of Fluid Engineering*, Vol. 108, June 1986.

[23] Shih, T.H.: An Improved $k - \epsilon$ Model for Near-Wall Turbulence and Comparison with Direct Numerical Simulation. NASA TM-103221, ICOMP-90-16, 1990.

[24] Shih T.-H.; Mansour N.N.: Modeling of Near-Wall Turbulence. *Proceedings of the International Symposium on Engineering Turbulence Modelling and Measurements*, September 24-28, 1990, Dubrovnik, Yugoslavia.

[25] Speziale, C.G.; Abid, R.; and Anderson, E.C.: A critical Evaluation of Two-Equation Models for Near Wall Turbulence. *AIAA paper* 90-1481, 1990.
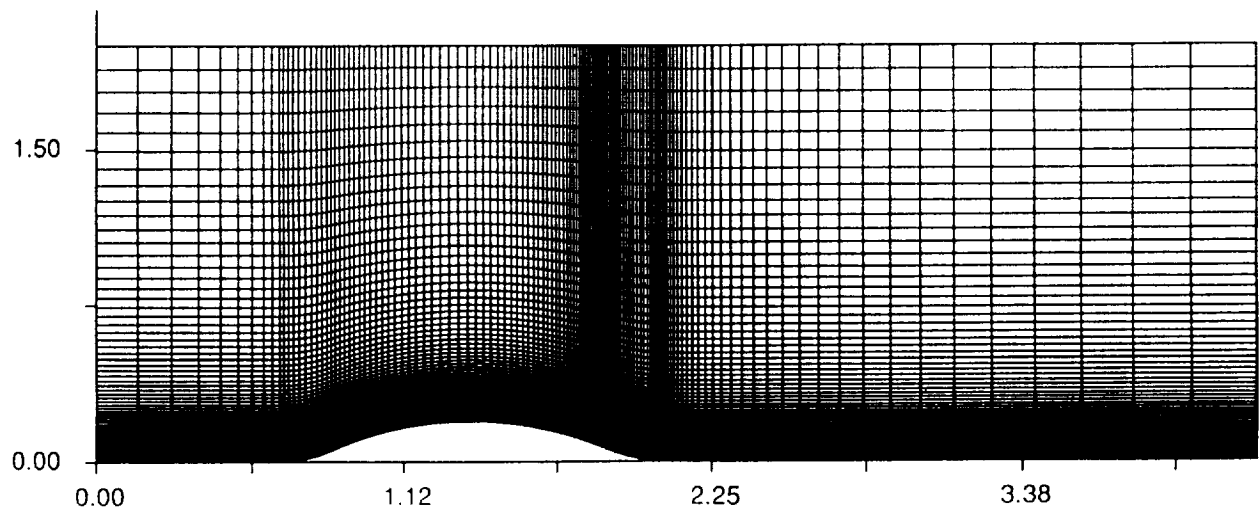
Figure 1: **Grid number 2 for the flow past a hill**
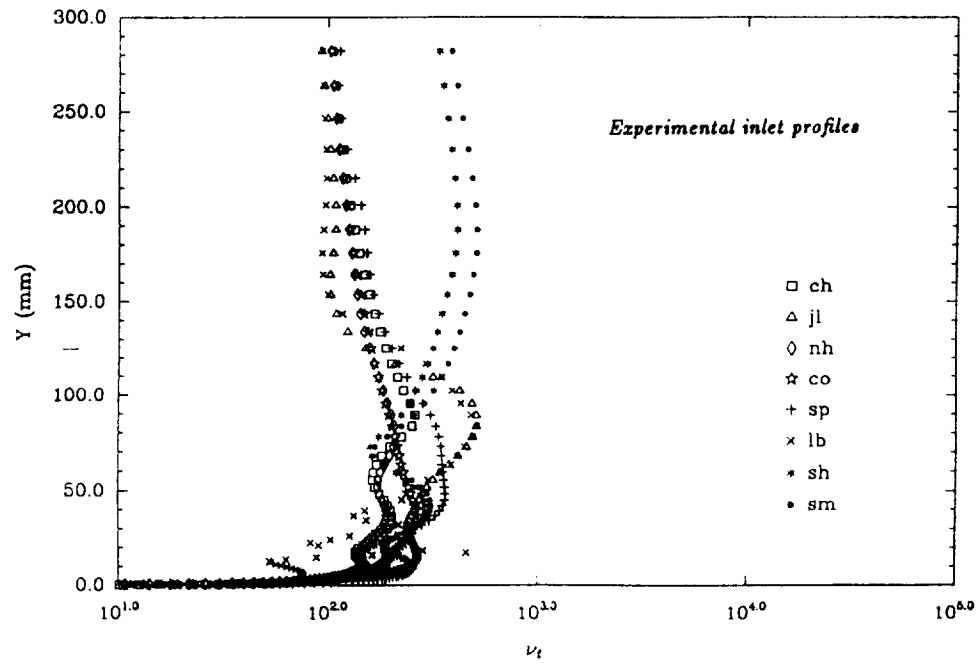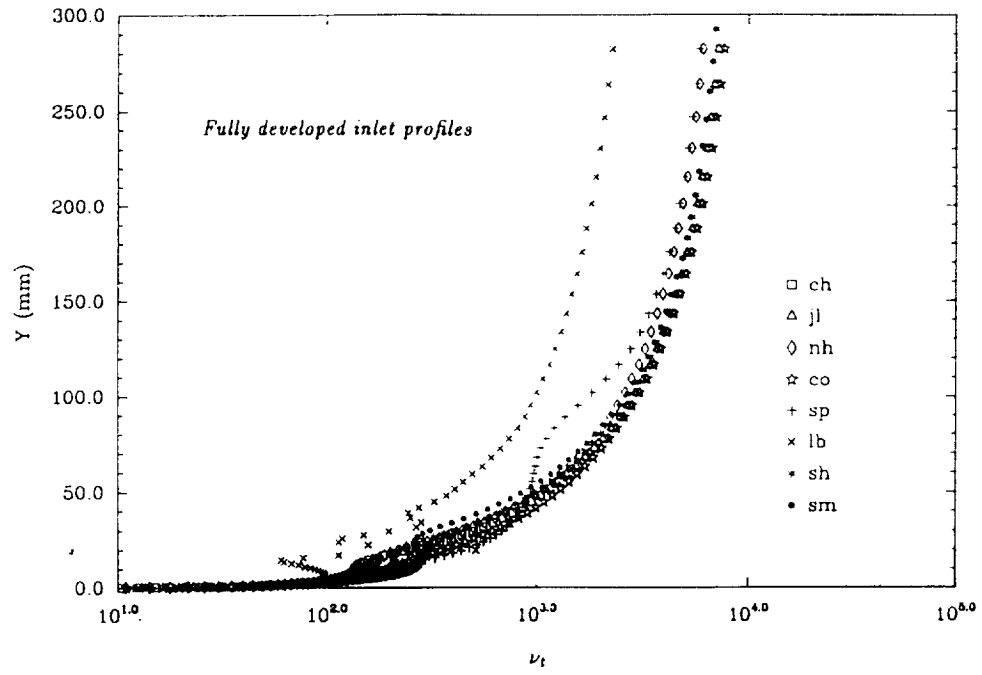
Figure 2: **Turbulent viscosities at** $X = 1990\,mm$
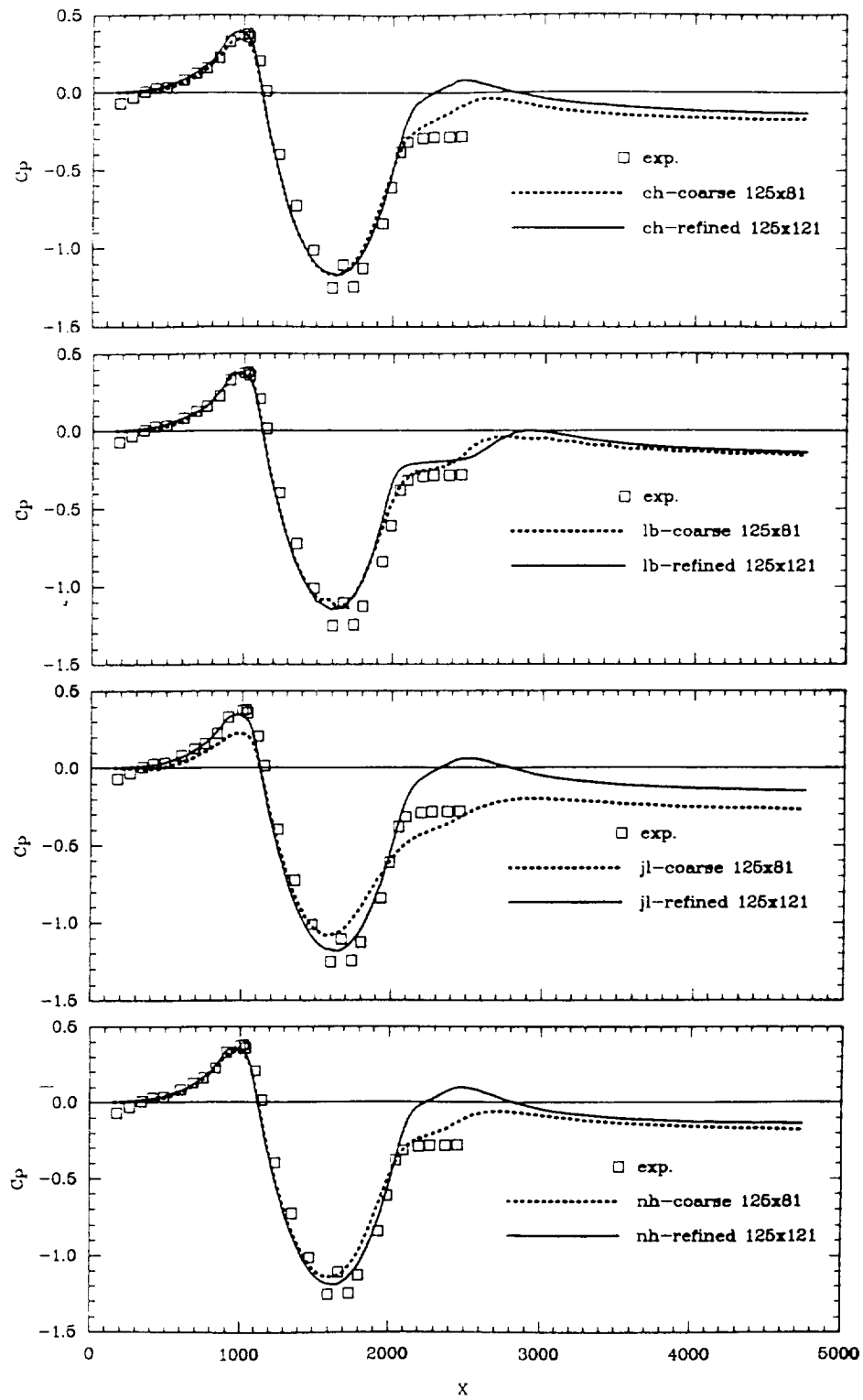
Figure 3: **Wall static pressure**
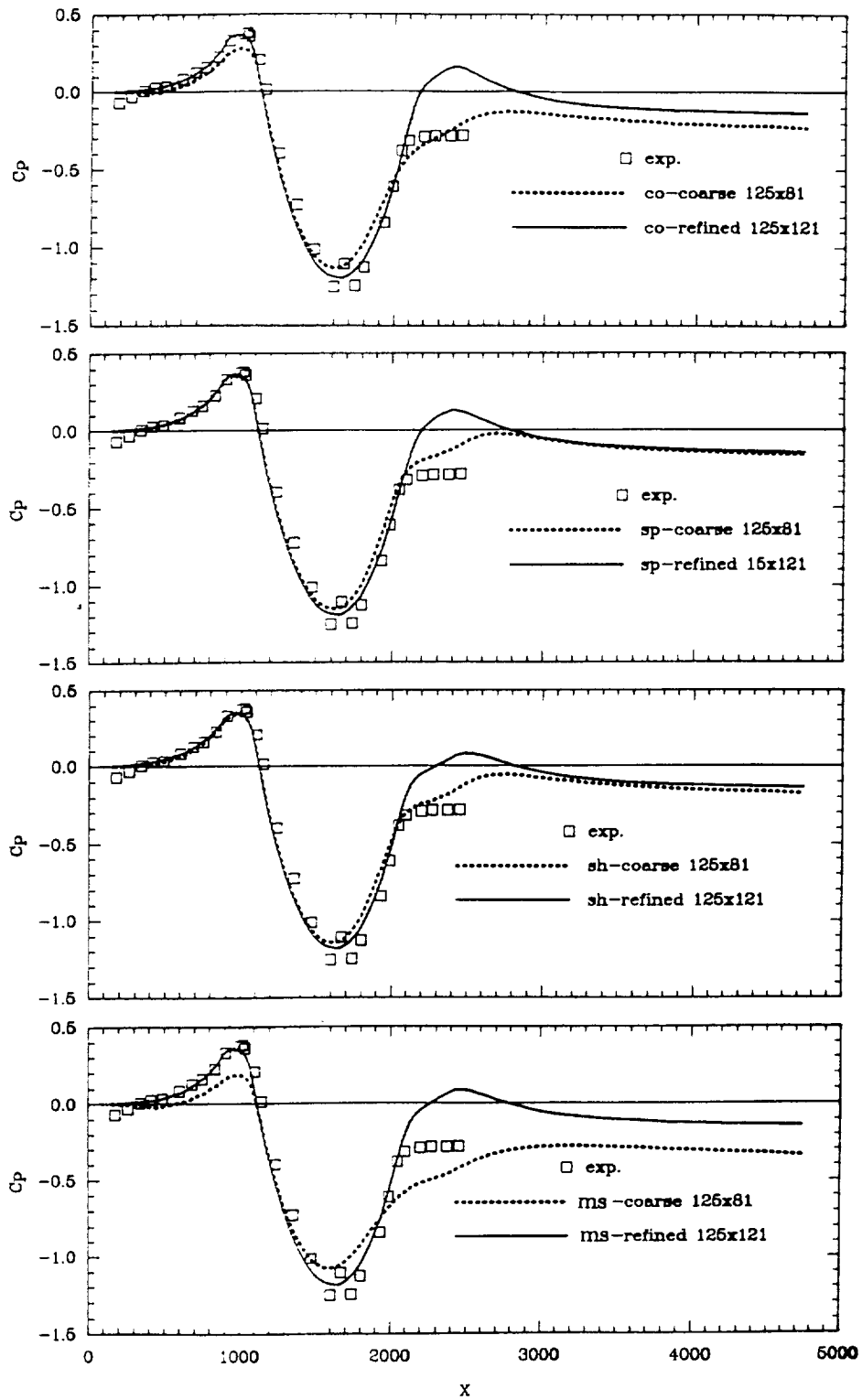
Figure 3: **Wall static pressure (contd)**
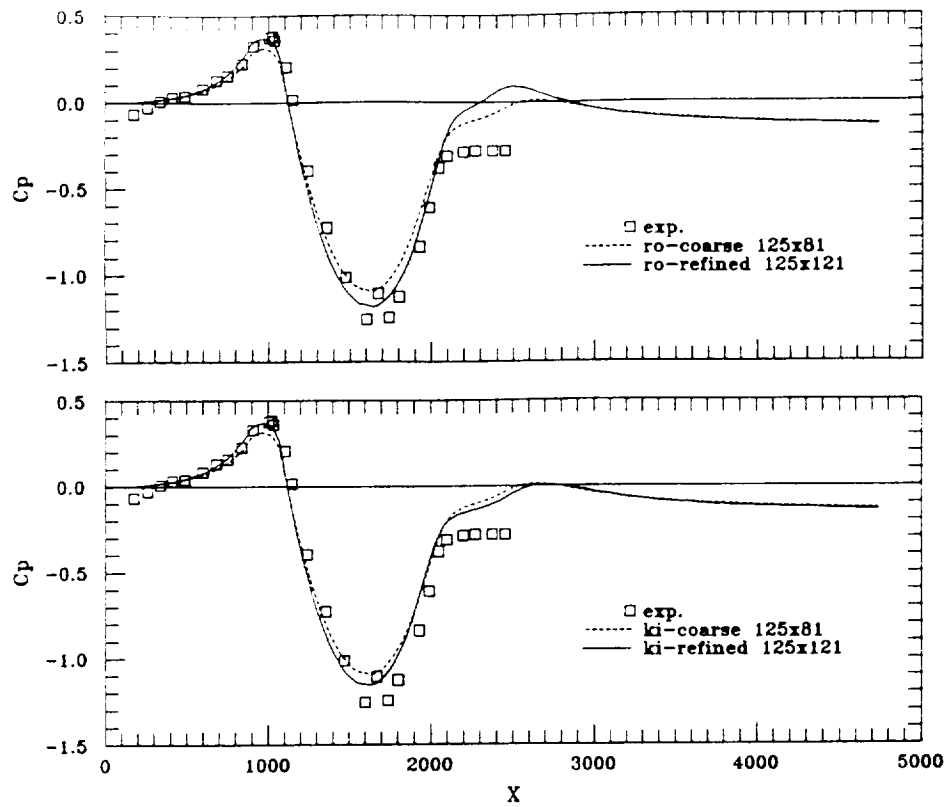
Figure 3: **Wall static pressure (contd)**
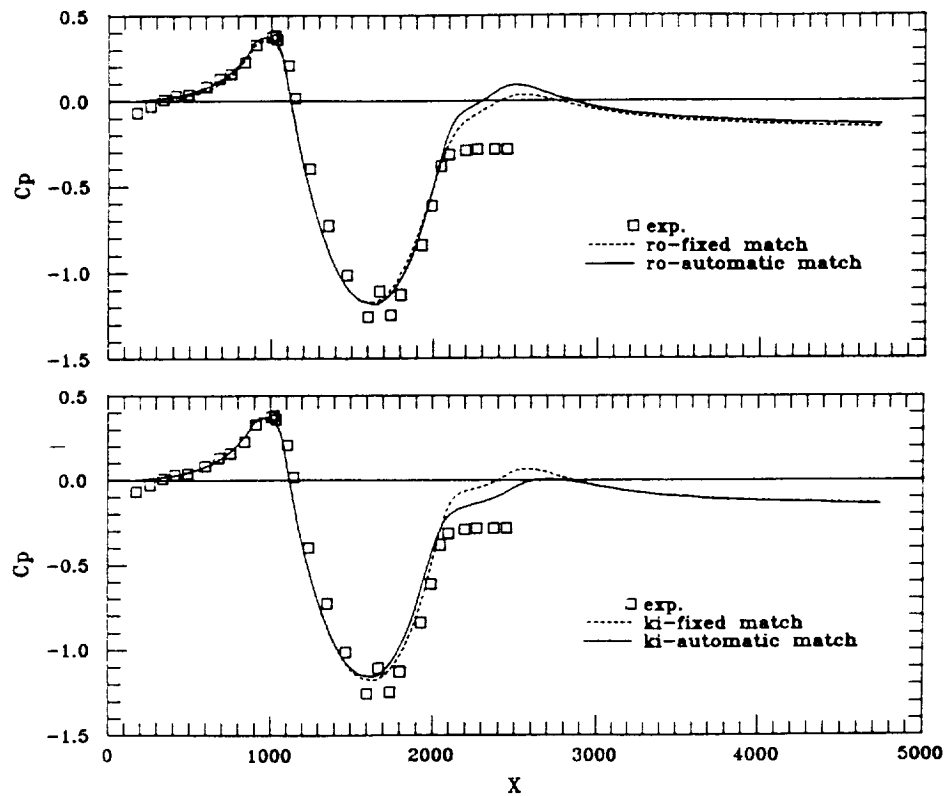
Figure 4: **Wall static pressure with different match levels**
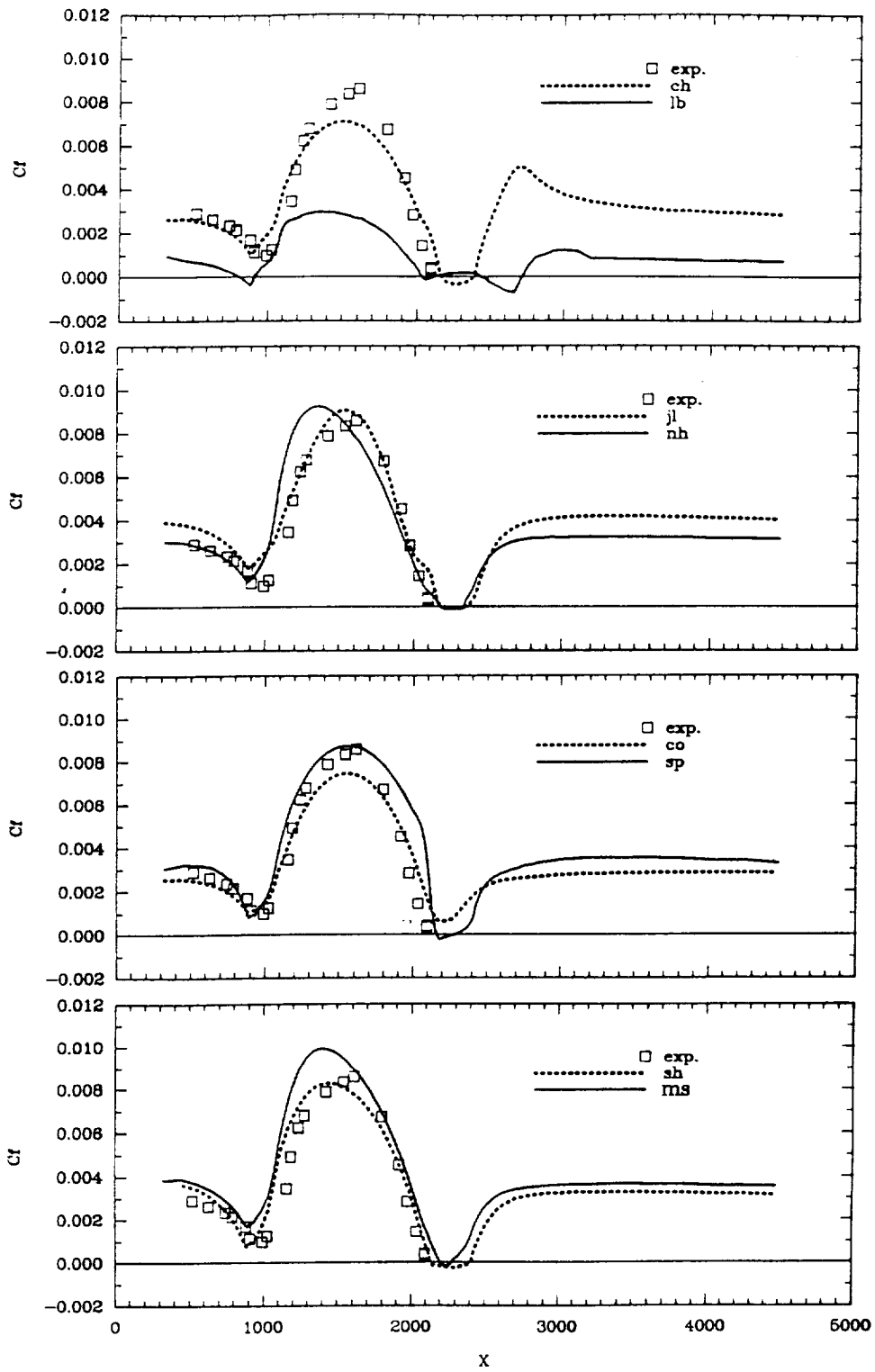
Figure 5: **Skin friction coefficient**
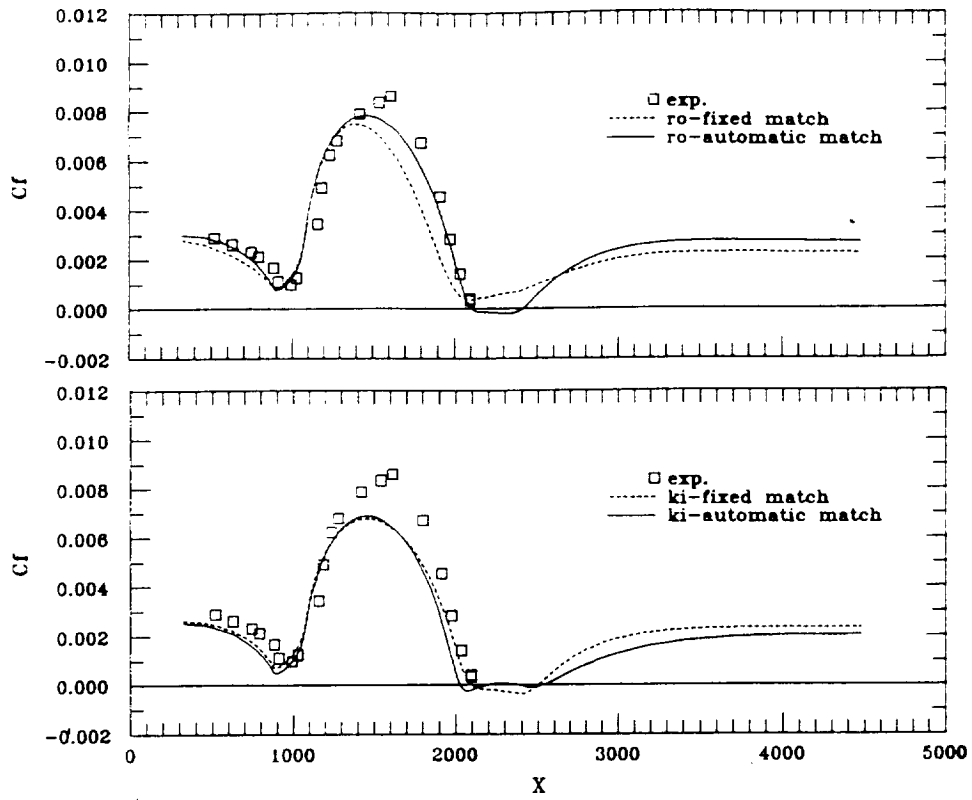
Figure 5: **Skin friction coefficient (contd)**
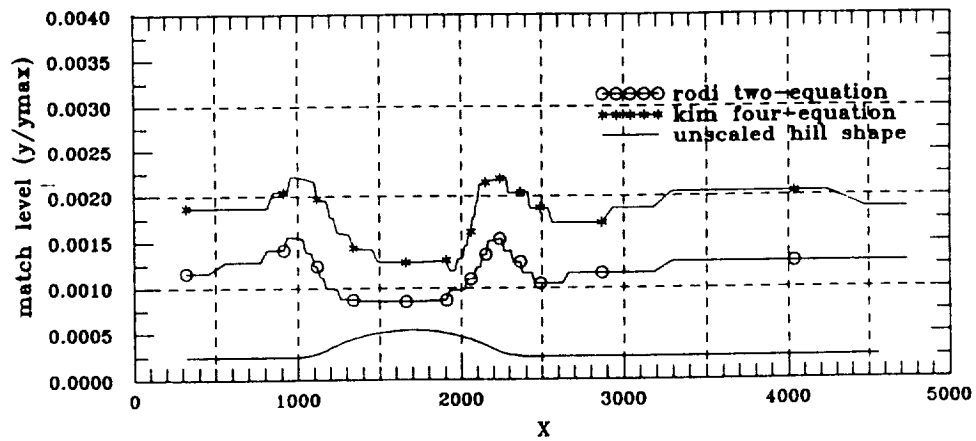
Figure 6: **Match level for two-layer models**
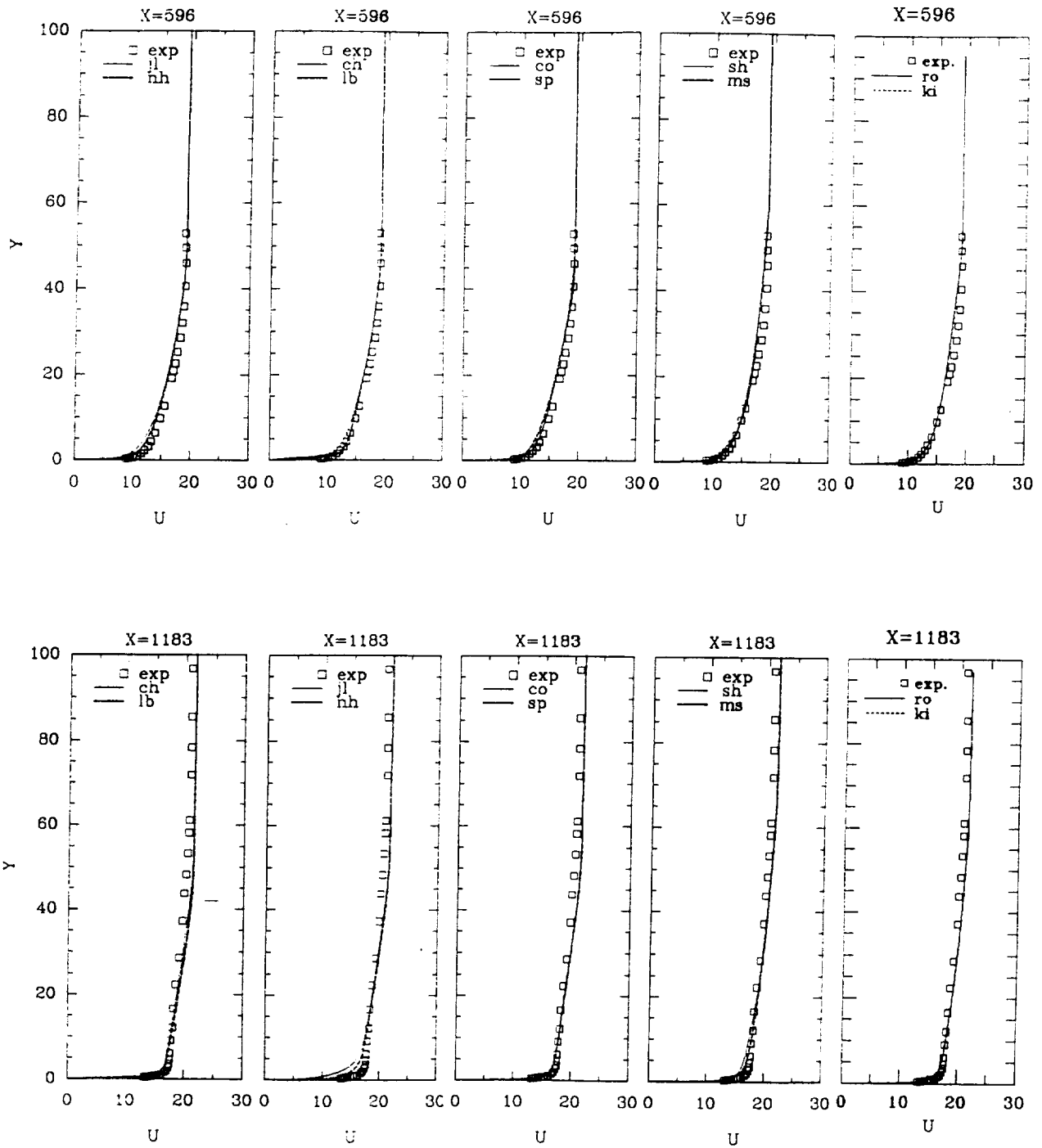
Figure 7: Cross sections: mean velocity
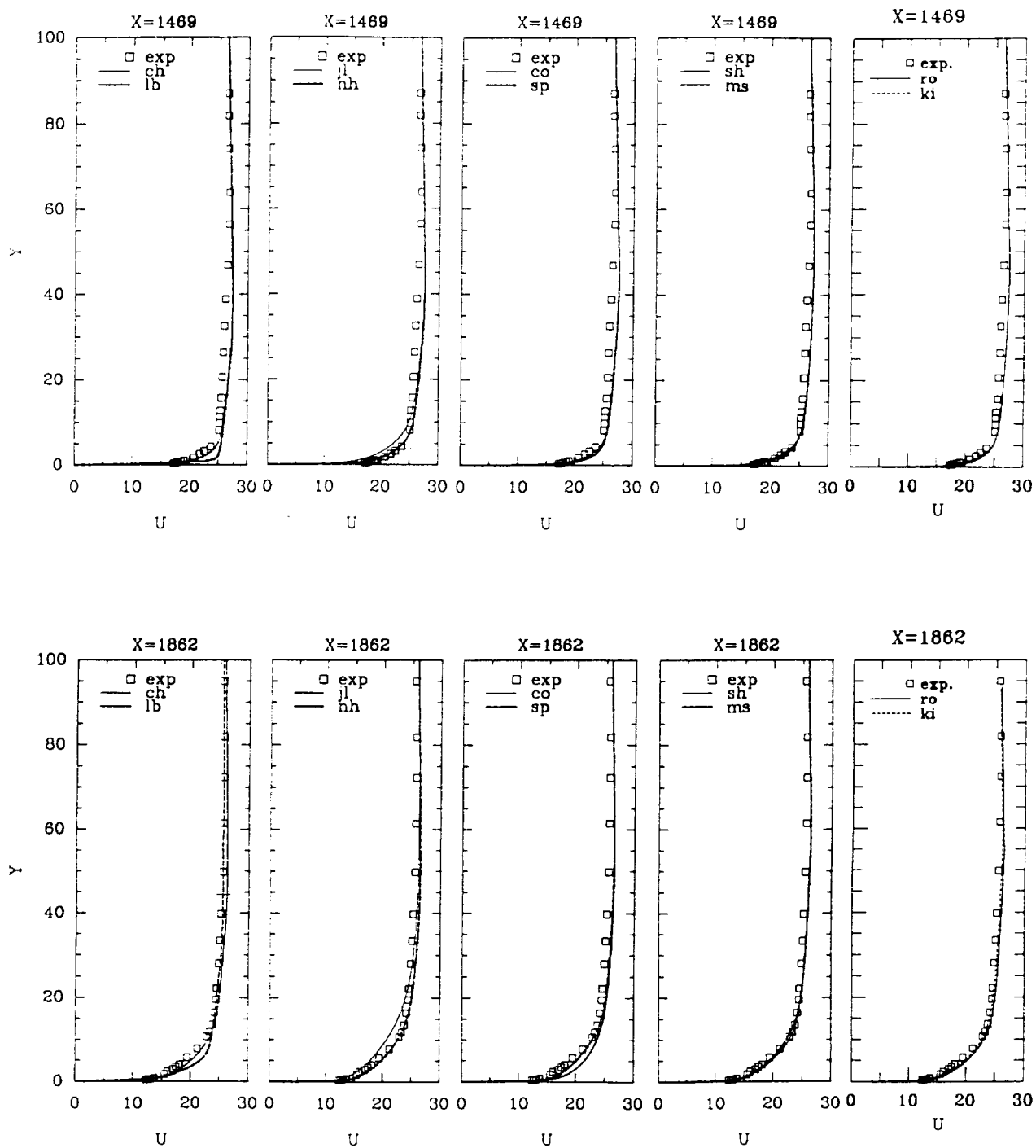
Figure 7: Cross sections: mean velocity (contd)
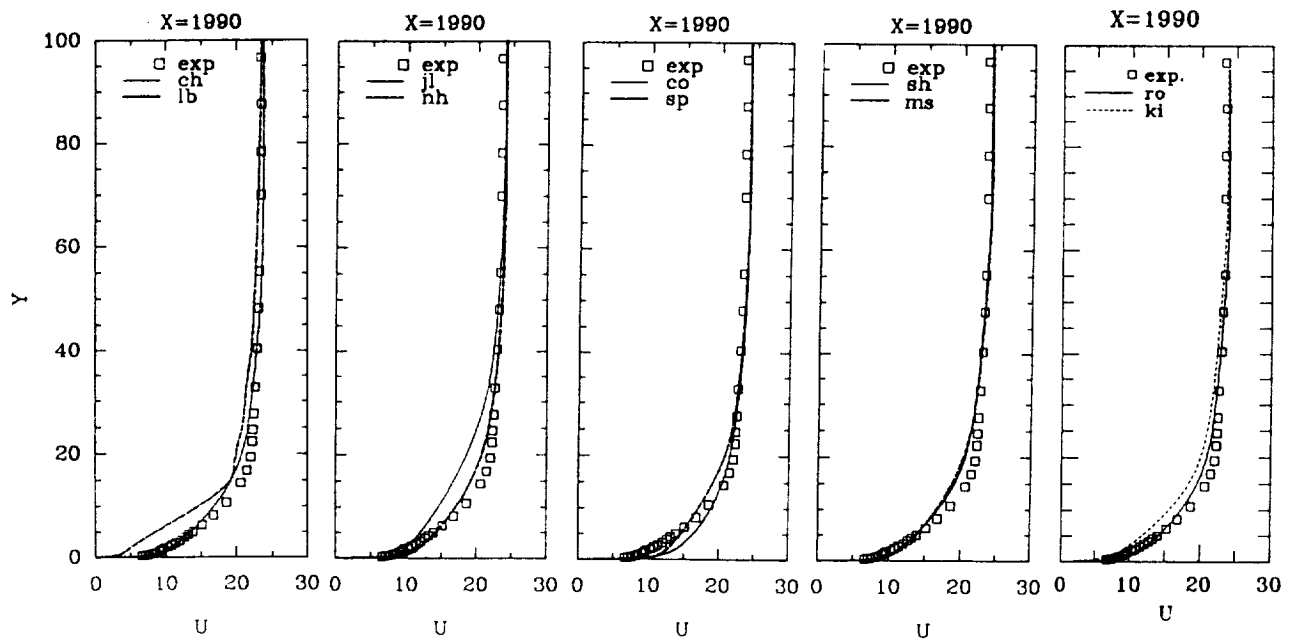
Figure 7: Cross sections: mean velocity (contd)
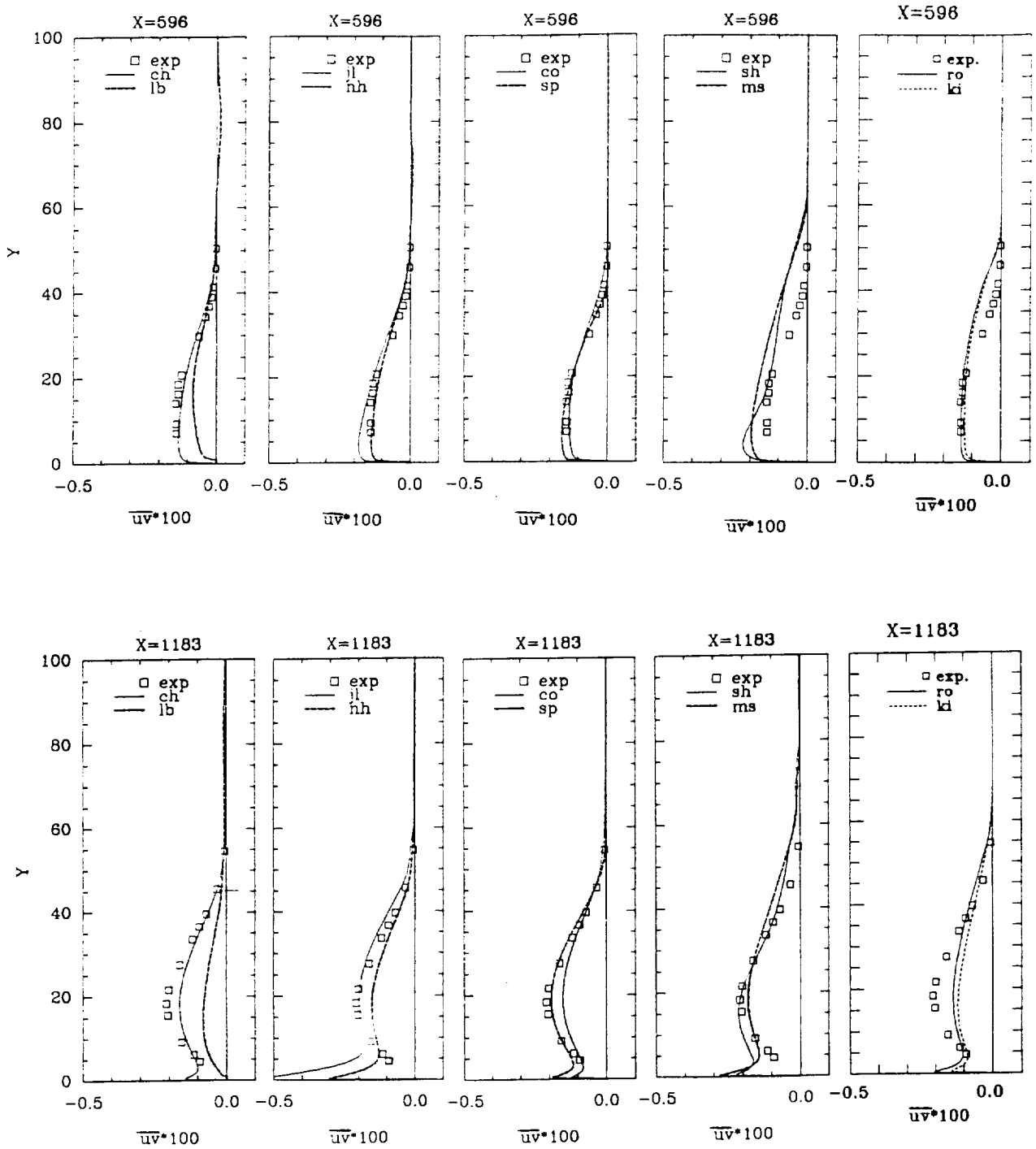
Figure 8: **Cross sections: turbulent shear stress**

Figure 8: Cross sections: turbulent shear stress (contd)

30
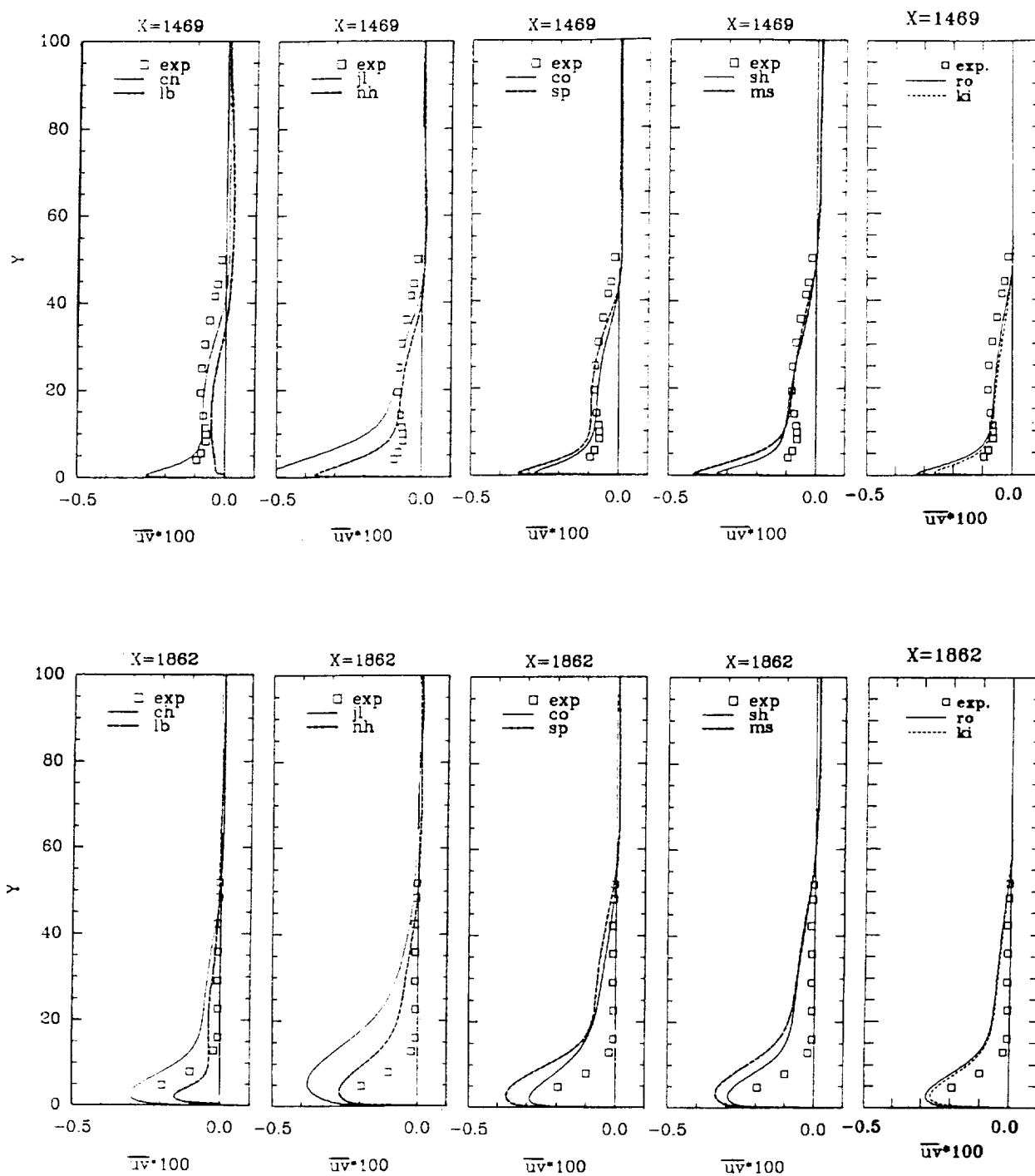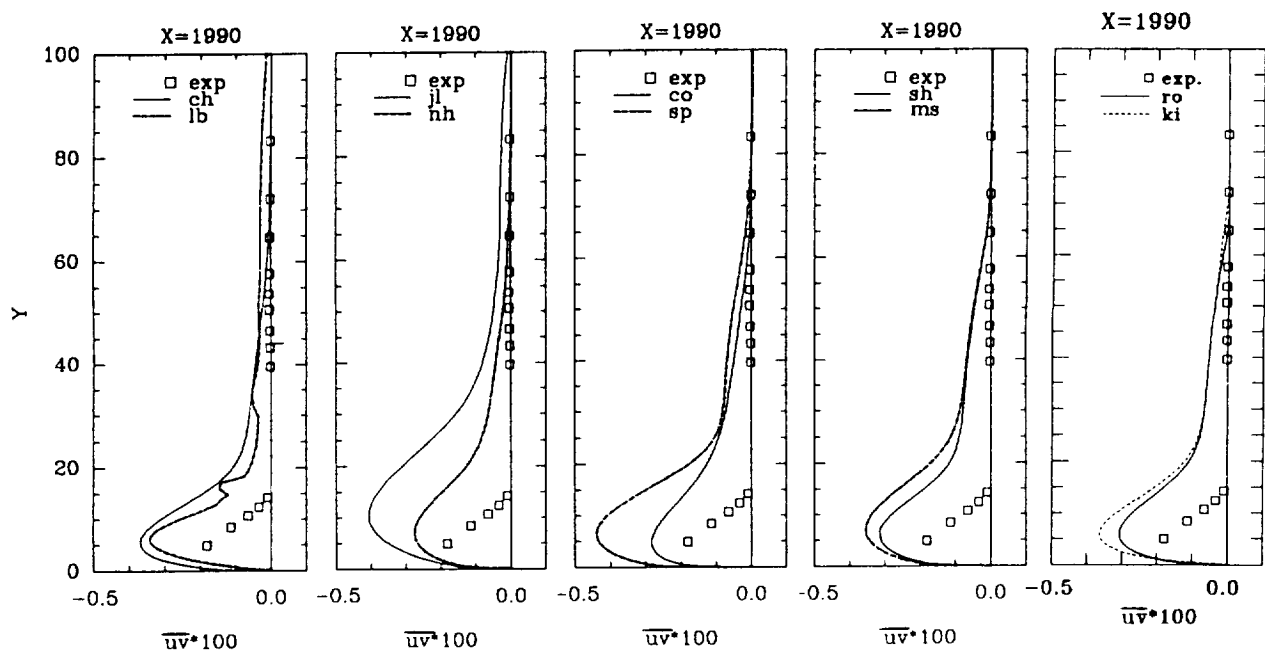
Figure 8: **Cross sections: turbulent shear stress (contd)**
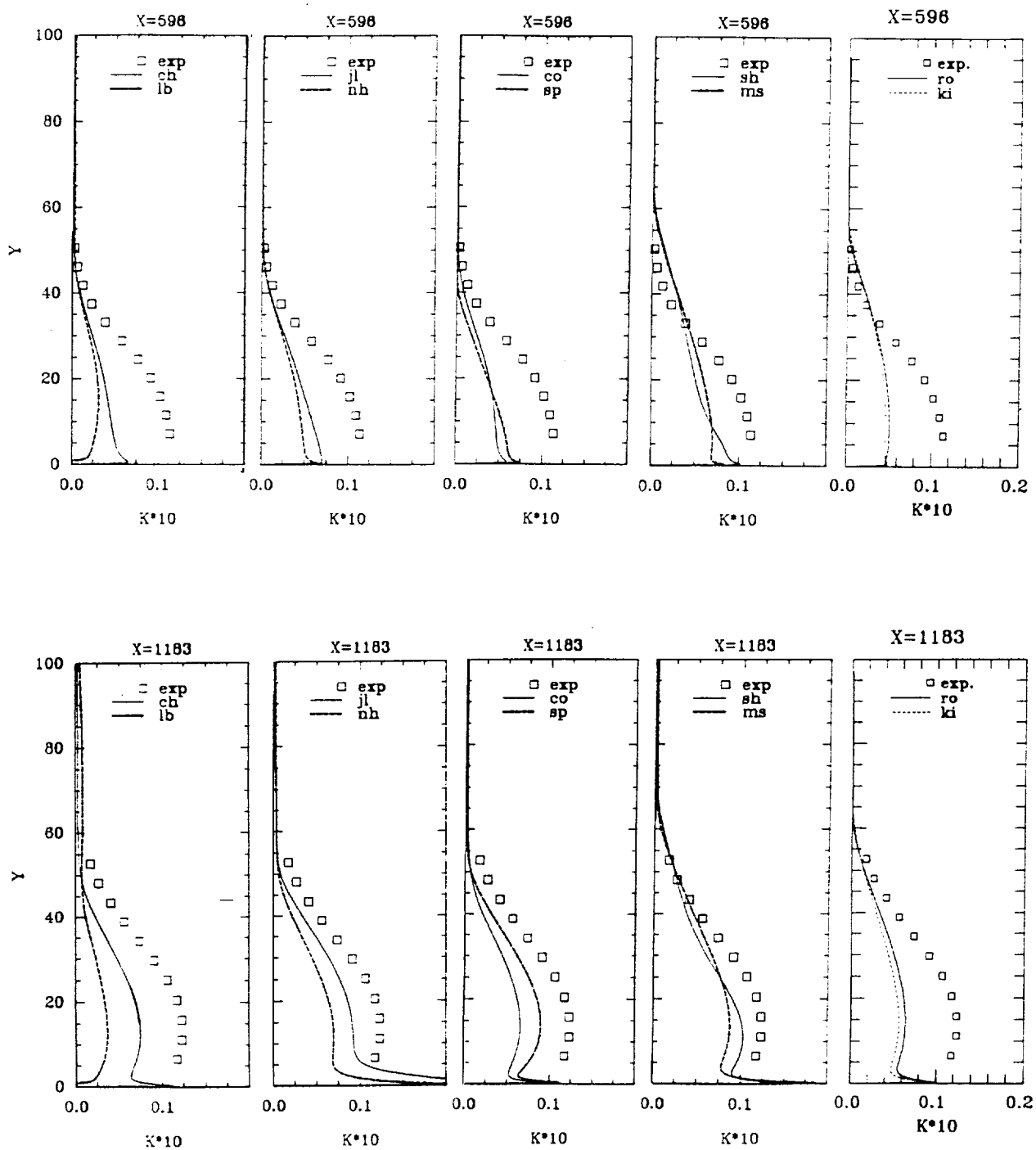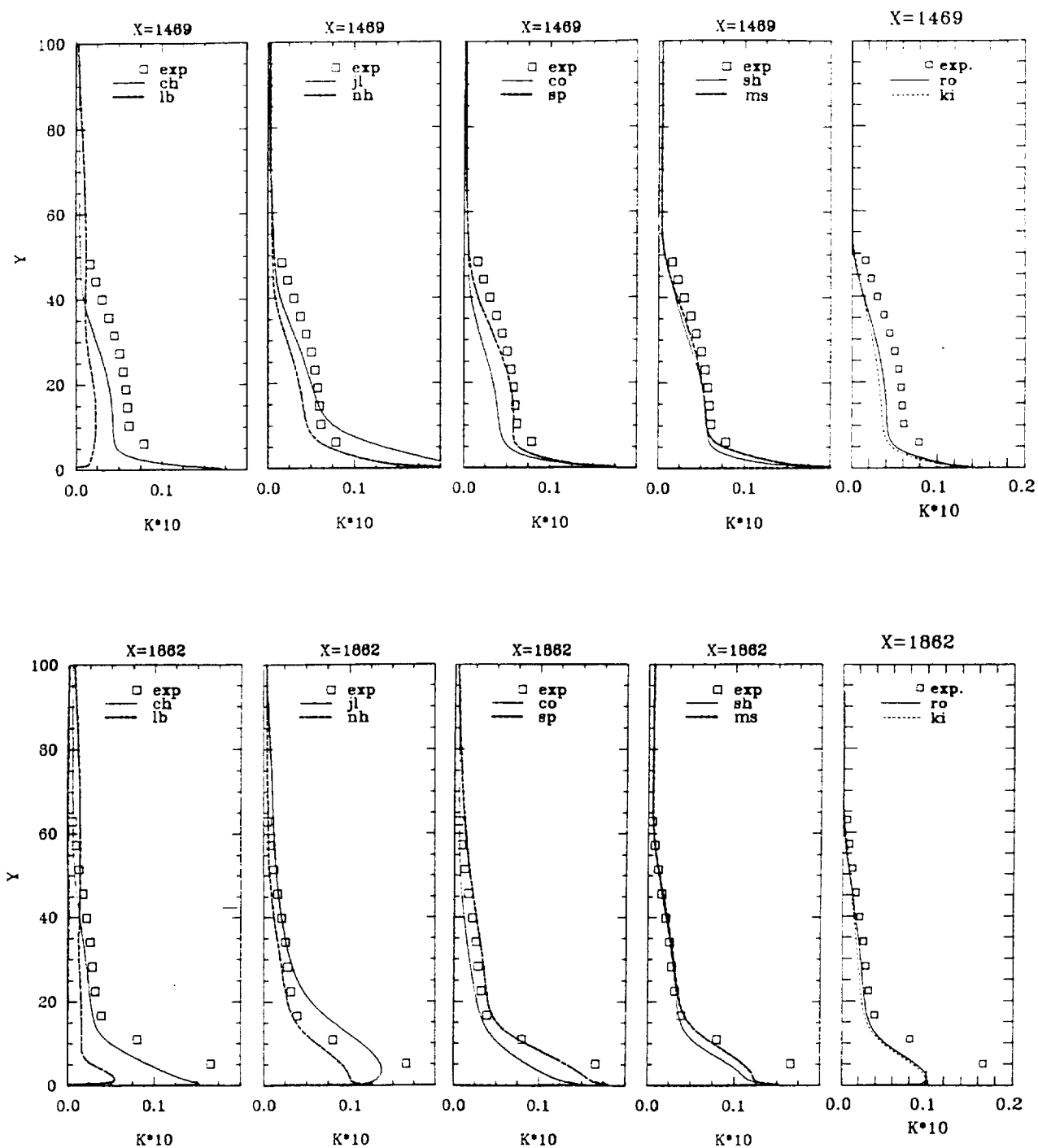
Figure 9: **Cross sections: turbulent kinetic energy**
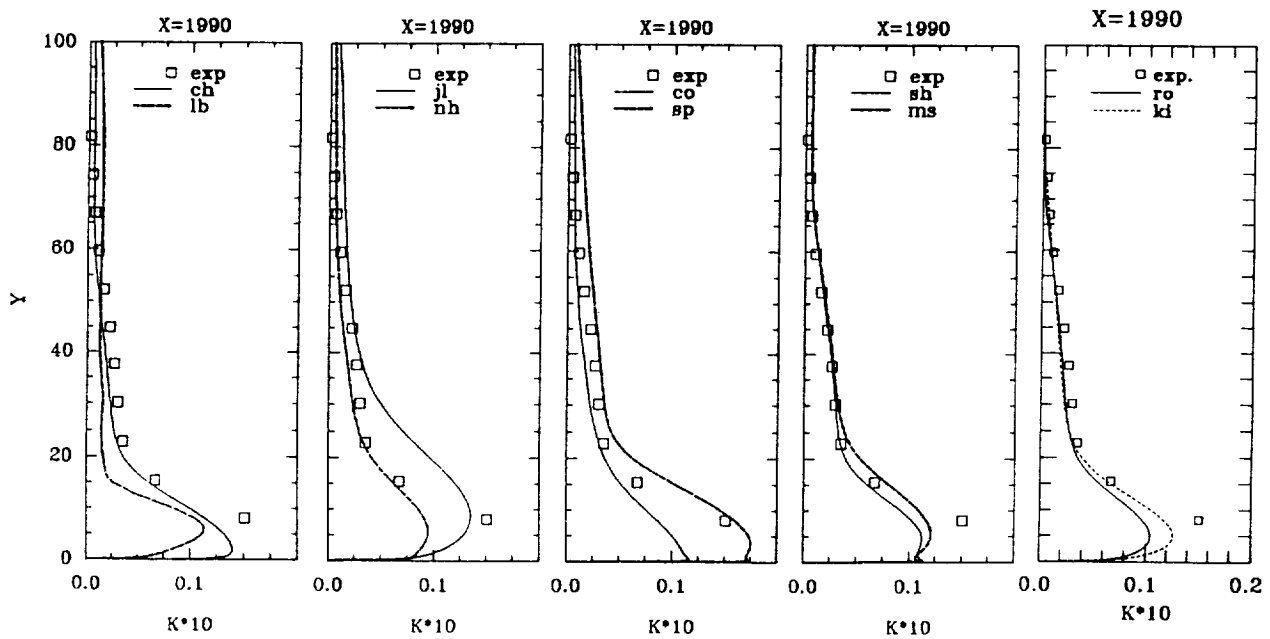
Figure 9: **Cross sections: turbulent kinetic energy (contd)**

Figure 9: Cross sections: turbulent kinetic energy (contd)

REPORT DOCUMENTATION PAGE

Public reporting burden for this collection of information is estimated to average 1 hour per response, including the time for reviewing instructions, searching existing data sources, gathering and maintaining the data needed, and completing and reviewing the collection of information. Send comments regarding this burden estimate or any other aspect of this collection of information, including suggestions for reducing this burden, to Washington Headquarters Services, Directorate for information Operations and Reports, 1215 Jefferson Davis Highway, Suite 1204, Arlington, VA 22202-4302, and to the Office of Management and Budget, Paperwork Reduction Project (0704-0188), Washington, DC 20503.

1. AGENCY USE ONLY (Leave blank)	2. REPORT DATE December 1991	3. REPORT TYPE AND DATES COVERED Technical Memorandum

4. TITLE AND SUBTITLE

Elliptic Flow Computation by Low Reynolds Number Two-Equation Turbulence Models

5. FUNDING NUMBERS

WU-505-62-21

6. AUTHOR(S)

V. Michelassi and T.-H. Shih

7. PERFORMING ORGANIZATION NAME(S) AND ADDRESS(ES)

National Aeronautics and Space Administration
Lewis Research Center
Cleveland, Ohio 44135-3191

8. PERFORMING ORGANIZATION REPORT NUMBER

E-6763

9. SPONSORING/MONITORING AGENCY NAMES(S) AND ADDRESS(ES)

National Aeronautics and Space Administration
Washington, D.C. 20546-0001

10. SPONSORING/MONITORING AGENCY REPORT NUMBER

NASA TM-105376
ICOMP-91-28
CMOTT-91-11

11. SUPPLEMENTARY NOTES

12a. DISTRIBUTION/AVAILABILITY STATEMENT

Unclassified-Unlimited
Subject Category 34

12b. DISTRIBUTION CODE

13. ABSTRACT (Maximum 200 words)

A detailed comparison of ten low-Reynolds-number k-ε models is carried out. The flow solver, based on an implicit approximate factorization method, is designed for incompressible, steady two-dimensional flows. The conservation of mass is enforced by the artificial compressibility approach and the computational domain is discretized using centered finite differences. The turbulence model predictions of the flow past a hill are compared with experiments at $Re = 1.4 \cdot 10^6$. The effects of the grid spacing together with the numerical efficiency of the various formulations are investigated. The results show that the models provide a satisfactory prediction of the flow field in the presence of a favourable pressure gradient, while the accuracy rapidly deteriorates when a strong adverse pressure gradient is encountered. A newly proposed model form that does not explicitly depend on the wall distance seems promising for application to complex geometries.

14. SUBJECT TERMS

Turbulence models; Low reynolds number; k-epsilon turbulence model

15. NUMBER OF PAGES
36

16. PRICE CODE
A03

17. SECURITY CLASSIFICATION OF REPORT Unclassified	18. SECURITY CLASSIFICATION OF THIS PAGE Unclassified	19. SECURITY CLASSIFICATION OF ABSTRACT Unclassified	20. LIMITATION OF ABSTRACT